High-resolution geodetic velocities reveal role of weak faults in deformation of Tibetan Plateau

Authors: T.J. Wright[1]*, G.A. Houseman[2,1], J. Fang[1]*, Y. Maghsoudi[3], A.J. Hooper[1], J.R. Elliott[1], L. Evans[4], M. Lazecky[1], Q. Ou[5], B.E. Parsons[6], J.C. Rollins[7], L. Shen[8], H. Wang[9], D. Wang[1]

Affiliations:

[1] COMET, School of Earth and Environment, University of Leeds, Leeds, UK

[2] State Key Laboratory of Deep Earth Exploration and Imaging, China University of Geosciences, Beijing, China

[3] COMET, Department of Earth and Environmental Sciences, University of Exeter, Penryn, UK

[4] School of Earth, Atmosphere & Environment, Monash University, Clayton, VIC, Australia

[5] COMET, School of GeoSciences, University of Edinburgh, Drummond, Edinburgh, UK

[6] COMET, Department of Earth Sciences, University of Oxford; Oxford, UK

[7] GNS Science, Lower Hutt, New Zealand

[8] Lamont-Doherty Earth Observatory, Columbia University, New York, USA

[9] College of Natural Resources and Environment, South China Agricultural University, Guangzhou, China

*Corresponding authors. Email: t.j.wright@leeds.ac.uk; j.fang@leeds.ac.uk

28 **High-resolution geodetic velocities reveal role of weak faults in deformation of**
29 **Tibetan Plateau**

30 **Authors:** T.J. Wright[1]*, G.A. Houseman[2,1], J. Fang[1]*, Y. Maghsoudi[3], A.J. Hooper[1], J.R. Elliott[1],
31 L. Evans[4], M. Lazecky[1], Q. Ou[5], B.E. Parsons[6], J.C. Rollins[7], L. Shen[8], H. Wang[9], D. Wang[1]

32 **Affiliations:**
33 [1] COMET, School of Earth and Environment, University of Leeds, Leeds, UK
34 [2] State Key Laboratory of Deep Earth Exploration and Imaging, China University of
35 Geosciences, Beijing, China
36 [3] COMET, Department of Earth and Environmental Sciences, University of Exeter, Penryn,
37 UK
38 [4] School of Earth, Atmosphere & Environment, Monash University, Clayton, VIC, Australia
39 [5] COMET, School of GeoSciences, University of Edinburgh, Drummond, Edinburgh, UK
40 [6] COMET, Department of Earth Sciences, University of Oxford; Oxford, UK
41 [7] GNS Science, Lower Hutt, New Zealand
42 [8] Lamont-Doherty Earth Observatory, Columbia University, New York, USA
43 [9] College of Natural Resources and Environment, South China Agricultural University,
44 Guangzhou, China

45 *Corresponding authors. Email: t.j.wright@leeds.ac.uk; j.fang@leeds.ac.uk

46 **Abstract:**

47 Understanding the key mechanisms that control the tectonic deformation of the continents
48 remains a fundamental challenge in geodynamics. We present a high-resolution geodetic velocity
49 field of the Tibetan Plateau, which shows that a few major strike-slip fault systems separate
50 regions of more uniformly distributed deformation. We suggest that focused strain on major fault
51 systems is enabled by relatively low-viscosity ductile shear zones extending through the
52 lithosphere beneath the seismically active fault planes. Simple model calculations show that high
53 slip rates on the Kunlun Fault enable east-west extension to be distributed broadly across the
54 relatively weak southern and central Tibetan Plateau. Activation of the Kunlun fault in the
55 Miocene at the same time as onset of rifting in the north–south grabens suggests a causal
56 relationship.

57 **One-Sentence Summary:** New satellite data reveal how major fault systems influence the
58 tectonic deformation of the Tibetan Plateau.

59

60 Collision of the Indian tectonic plate with Eurasia over the last ca. 55 Ma has created an
61 extensive region of deforming crust that extends from the Himalayas in the south, through the
62 Tibetan Plateau, and into Central Asia (*1,2*). Continents deform through a combination of
63 continuous distributed deformation and focused strain on lithospheric-scale faults (*3-6*). Much of
64 the small-scale seismic activity in regions of continental deformation can be explained by a
65 relatively superficial crustal layer comprised of minor crustal blocks that are carried along by a
66 ductile substrate (*7*). However, it has long been clear that relatively few major fault zones (*8*)
67 have a significant effect on continental deformation and seismic hazard. The importance of these
68 major fault zones in controlling the overall deformation field has been difficult to assess given
69 the limited spatial resolution of available geodetic displacement maps. We here document a
70 large-scale compilation of geodetic data for the Tibetan Plateau that quantifies how the

deformation field of the India–Eurasia continental collision is controlled by a combination of both long-wavelength continuous deformation and strain focused on a few major fault systems. Better models of how the continents deform are important for seismic hazard assessment as they determine the degree to which earthquakes are focused on closely monitored major faults or occur on minor faults, which are often of unknown significance (*9*). Dynamical models that incorporate focused deformation on the major fault systems using the concept of a fault resistance coefficient (*10*) provide new quantitative constraints on the deep ductile shear zones inferred from diverse lines of evidence (*11*), and evident now in offset structure in the mantle beneath crustal faults (e.g. *12*).

The Tibetan Plateau is the world's largest region of continental deformation and has long been the testing ground for models of continental tectonics (e.g., *13-16*). As geodetic observations, particularly from Global Navigation Satellite Systems (GNSS), have improved (e.g., *17*), models have been refined, with recent kinematic models resolving elastic deformation within blocks and fault-slip rates on their boundaries (e.g., *18*). However, ground-based GNSS observations remain relatively sparse in parts of the Tibetan plateau (e.g., *19*). With 10 years of observation from the Sentinel-1 radar constellation (*20*) and, as a result of advances in Interferometric Synthetic Aperture Radar (InSAR) processing (*21, 22*), we compiled near-complete maps of present-day displacement and strain rates across the Tibetan Plateau. These maps provide the level of detail required to quantify the relative importance of continuous ductile deformation and localized discontinuous displacement on the major fault systems. The plateau is largely the consequence of crustal thickening due to north–south convergence but is now extending in an approximately east–west direction (*23*). The extension is caused by excess gravitational potential energy of the plateau (*24*); our data and models show the critical role of major fault systems in controlling the spatial distribution and rate of both north-south shortening and east-west extension.

Surface velocities and strain rates

To map surface velocities at high resolution, we first produced a network of short-baseline Sentinel-1 interferograms in 127 ascending and 114 descending frames covering the Tibetan Plateau (Fig. S1) using the COMET-LiCSAR system (*21*), spanning 2016 to 2024. More details of our approach are given in the Supplementary Materials (*SM*). We used the LiCSBAS algorithm (*22,25*) to compute average line-of-sight surface velocities for each frame (*SM.1-2*). To avoid contamination, we removed signals from coseismic deformation for earthquakes larger than M_w 6 before calculating the average velocities (*SM.3*). Line-of-sight velocities for each frame were initially independently referenced. Then we used a compilation of GNSS velocities and levelling data (*SM.4;* Fig. S2) to jointly invert for reference frame adjustment parameters and smooth 3D velocities on a ~0.2° triangular mesh (Fig. S1), following (*26,27*) (*SM.5*; Fig. S3), hereafter referred to as the *coarse* velocity model. The inverted reference frame parameters allowed us to derive mosaics of ascending and descending line-of-sight velocities tied to the Eurasian reference frame (Fig. S4). Following (*28*), we used the Eurasian line-of-sight mosaics to solve for east–west (Fig. 1) and vertical (Figs. 2B, S5) velocities at 1 km resolution in areas where both ascending and descending data exist, using the north–south velocities from the *coarse* velocity model (Fig. 2A) as a constraint. The spatial gradients of the horizontal velocities were used to derive horizontal strain rates and rotation rates in a spherical coordinate system (*SM.5*; Figs. 2, S6-8). Uncertainties in the velocities are generally less than 2 mm/yr, as described in (*SM.6;* Figs. S3, S9-12).

The horizontal velocity and strain-rate fields (Figs. 1, 2) reveal how the Tibetan Plateau is deforming in response to northward motion of the Indian plate. The broad-scale deformation pattern is consistent with previous studies (e.g. *19, 29*) that show plateau shortening in a direction parallel to the plate-motion convergence vector of India relative to Eurasia and also extending perpendicular to this direction (Fig. 1). South of the Kunlun fault, extension outpaces convergence, resulting in dilatation and likely crustal thinning (Fig. 2), consistent with inference from earthquake mechanisms (*23*).

The vast majority (95%) of inverted vertical velocities (Fig. 2) in the plateau fall in the range +/- 5 mm/yr; this range is only slightly larger than our estimate of uncertainty in the vertical velocities ($2\sigma \approx 3$ mm/yr; Fig. S11). Short wavelength components of the vertical velocities are in some cases correlated with topography and can be attributed to surficial processes including loss of permafrost, hydrological changes, and anthropogenic activity (*30*), as well as potential contamination from phase biases (*31*). Longer wavelength vertical signals are largely controlled by GNSS and levelling observations (Fig. S13); these are generally larger than can be explained by horizontal lithospheric tectonics. For example, the dilating region south of the Kunlun fault (outlined in Fig. 2D) has an average rate of dilatation of 6 nanostrain/yr; assuming isostatic balance operates on long wavelengths, we obtain a subsidence rate of < 0.1 mm/yr. The disconnect between horizontal tectonics and observed vertical motions is also evidenced by the lack of correlation between vertical rates and the dilatation field (Fig. 2). An exception is where we see uplift associated with interseismic elastic deformation on Himalayan thrust systems (*32*). Vertical motions likely arise primarily from permafrost (*30*), hydrological loading (*33*), glacial isostatic adjustment (34), and deeper mantle processes (*35*).

Compared to GNSS-derived strains (Fig. S14), the inclusion of InSAR data in our velocity field sharpens the spatial resolution of deformation observations, particularly in the interior of the plateau (Figs. 2, S6-8), where the gradients in east–west velocities (well resolved by InSAR) are highest. The strain-rate field clearly demonstrates that the highest strain rates in the plateau interior are focused on major strike-slip fault systems: the Altyn Tagh, Kunlun, Haiyuan, and Xian Shui He faults (Fig. 2). Velocity profiles not crossing these major fault systems do not in general show significant strain concentrations associated with minor mapped faults (Fig. 1). The major fault systems separate regions of relatively low strain rate; however, the second invariant of the strain rate tensor in the plateau interior (region shown on Fig. 2D) is still relatively high, with a median value of 24 nanostrain/yr, compared to typical values of 2–3 nanostrain/yr in stable continental regions (*36*) and significantly higher than the 9 nanostrain/yr we estimate in the Sichuan basin (*SM.6*). The eastward displacement of the plateau is associated with diffuse east–west extension in the south–central Tibetan Plateau, and outward flow and rotation (Fig. S7) around the eastern Himalayan syntaxis (Fig. 1). In the northeastern Tibetan Plateau, north–south contraction implies crustal thickening and active topographic growth (*30,37*).

Several of the fault systems within the plateau have been affected by earthquakes in the 20-year period before the Sentinel-1 observations, including the 1997 M_w 7.4 Manyi and 2001 M_w 7.8 Kokoxili earthquakes, on the Kunlun Fault and its westward extension, and the 2008 M_w 7.2 and 2014 M_w 6.9 Yutian earthquakes, associated with the westward termination of the Altyn Tagh fault (Fig. 1). We observe elevated post-seismic strain rates where the faults slipped in those recent events (Fig. 2). These include both localized shear strains and dilatations, with the Yutian Fault showing apparent areal dilation and the Kokoxili/Manyi ruptures showing apparent contraction. It is important to note that high strain rates occur elsewhere on major fault systems

160 in locations where there were no recent earthquakes. For example, there is no known historic
161 rupture of the Kunlun fault east of 100°E (*38*), but shear strain rates remain high on the fault. We
162 interpret the high-strain rates observed away from recent ruptures as being characteristic of the
163 inter-seismic part of the earthquake cycle (*39*). Previous studies of the earthquake deformation
164 cycle on other major strike-slip fault systems have shown that steady, high inter-seismic strain
165 rates are reached following a few decades of elevated post-seismic strain rates (*40-42*).

Geodynamic modelling

167 We developed a quantitative dynamical model to explain the observed deformation field. We
168 adapted the thin viscous sheet model (*13*) by including fault-like discontinuities at pre-defined
169 locations and solved for the displacement-rate field represented on a spherical shell in a regional
170 domain that covers the Tibetan Plateau and most of the Central Asia collision zone (*10,43;* Fig.
171 3A). Model faults were defined based on zones of localized shear (Fig. 2C). Thus, we included a
172 simplified representation of the Kunlun, Haiyuan, Altyn Tagh, Sagaing, and Xian Shui He faults.
173 In the model, horizontal displacement rates are independent of depth, and stresses were averaged
174 across the thickness of the lithosphere, so that we obtained a two-dimensional representation of
175 the instantaneous horizontal velocity field from which we derived the strain-rate distribution. We
176 assumed that the thin viscous shell deforms according to a depth-averaged non-linear constitutive
177 law,

$$\tau_{ij} = B\dot{E}^{(1-n)/n}\dot{\varepsilon}_{ij}, \text{ where } \dot{E} = \sqrt{\dot{\varepsilon}_{ij}\dot{\varepsilon}_{ij}} \tag{1}$$

179 in which deviatoric stress τ is a function of strain-rate, $\dot{\varepsilon}$, and depth-averaged viscosity
180 coefficient, B. Eq (1) is a frame-invariant statement of the simplified idea that strain-rate varies
181 as the *n*th power of depth-averaged deviatoric stress. We assumed *n = 3*, a typical value for
182 olivine (*44*), which comprises the major mineral of the mantle lithosphere, but is also
183 representative of the vertically averaged stress vs strain-rate relation (*45*). In our simplified
184 depth-averaged model of the lithosphere at continental scale, we represented each major fault as
185 a discontinuity in which the horizontal traction component acting on the fault plane (tangential σ_t
186 or normal σ_n) is proportional to the discontinuity in displacement rate across the fault (tangential
187 Δu_t, or normal Δu_n), considered an average rate over multiple earthquake cycles:

$$\sigma_t = f_t \Delta u_t; \sigma_n = f_n \Delta u_n \tag{2}$$

190 The proportionality constants (fault-resistance coefficients f_t, f_n) similarly represent a depth-
191 average of the resistance to localized relative displacement in strike-parallel (or strike-
192 perpendicular) direction. The fault resistance coefficient is a convenient way to characterize the
193 behavior of an active fault zone system without prejudging its value, or its variability, on a
194 particular fault.

195 We obtained apparent values of *f* on specific faults in this calculation by adjusting *f* until there
196 was a good match to the geodetic velocity field. Thus, with this relatively simple model we could
197 examine the effect of allowing localized shear strain on lithospheric-scale fault systems within a
198 continuously deforming region.

199 Boundary conditions on the external edges of the model domain (Fig. 3A; S15) simulate the
200 relative plate rotations of India (*46*) and the Yangtze and Amur plates (*47*) with respect to
201 Eurasia. The force balance includes the effect of spatially variable gravitational potential energy,

202   here calculated assuming local isostatic balance of topography from ETOPO1 (*48*) smoothed
203   with a 20-km-wide Gaussian filter.

204   We assumed that the viscosity coefficient *B* in Eq. (1) can vary spatially (Fig. 3A). The reference
205   value of *B* that applies in the far-field (B_0) is constrained by the Argand number, *Ar*, which scales
206   the relative magnitude of viscous stress in the collision zone to the stress differences caused by
207   variations in gravitational potential energy (*13*). In regions representing India, and the Tarim,
208   Sichuan and Alashan-Ordos basins, we set $B = 10B_0$ so the regions would behave like nearly
209   rigid blocks within the deforming domain (Fig. S15). We constrained the various free parameters
210   (*Ar*, regional *B* values, and fault resistance coefficients *f*) by extensive numerical
211   experimentation in which we minimized the misfit between observed and model geodetic
212   velocities (*10*). From these experiments we determined that the Tibetan Plateau and Tian Shan
213   regions have a lesser viscosity coefficient ($0.3B_0$) and south-central Tibet is required to be even
214   weaker ($0.1B_0$; Fig. S15). Although the requirement for a low viscosity plateau region (*10*) is
215   necessary to fit the geodetic strain-rate field, it is consistent with the history of extensive
216   volcanism and magmatism across the plateau (*49*, *50*) and geophysical observations of low
217   shear-wave velocities and high electrical conductivity in the Tibetan upper crust (*51*), which
218   suggest extensive zones of partial melt and hydrothermal activity.

Implications for fault strength

220   Model calculations show that changes to *f* on a given active fault change the velocity field over
221   distances comparable to the length of the fault. The best fit to observed present-day velocity field
222   requires different *f* values for different faults, but in general the major fault systems are relatively
223   weak (Fig. S15). When *f* is small on east-west oriented fault systems like the Kunlun the result is
224   significantly increased eastward velocities south of the fault (Figs. 1, 3A,B). Transient
225   postseismic deformation can also impact estimates of *f*. For example, the velocity change across
226   the western end of the Kunlun Fault, which was impacted by the Kokoxili and Manyi
227   earthquakes, is best matched using $f = 0$; whereas the unimpacted eastern half of the fault
228   requires a higher, but still small, value of *f* (i.e., dimensionless $f' = 0.5$, with scaling defined in
229   (*10*); Fig. S16-17).

230   To illustrate why the Kunlun fault system has such a large impact on east–west extension over
231   most of south-central Tibet, we show (Figs. 3C,D,E, *SM.7*, S18,S19) a simplified mechanical
232   model that reduces the problem to its essential elements: a rectangular region of north–south
233   extent *W* and viscosity $\eta = B_0/2$ (with *n*=1) bounded to the north by a major strike-slip fault and
234   driven into extension by a contrast in gravitational potential energy on its eastern boundary.
235   Solutions obtained for this simplified model show the primary role of *f* that applies to the
236   northern boundary of the rectangular domain (Figs. 3D,E, S18, S19), representing the Kunlun
237   Fault. For $f = \infty$ (Fig. 3D), equivalent to a rigid northern boundary, solutions imply that
238   extension is locally restricted to near the eastern boundary. By contrast, in solutions with a
239   dimensionless fault resistance parameter $f' = 0.5$ or less (with $f' = \frac{Wf}{\eta}$ in the simplified model),
240   representing a weak fault, the extensional strain-rate field spans most of the region (Fig. 3C;
241   S18). The simple model and related analytical solutions explain the length scales of the
242   systematic northward and eastward increase in the east component of geodetic velocities (*SM.8*).

243   Comparing observed north–south profiles of the eastward velocities (e.g. Figs. 1C, 3F) with
244   predictions of the simplified model (Fig. 3, S19) shows that the apparent value of *f'* on the
245   Kunlun fault system must be less than ~0.5. For an effective viscosity of the lithosphere in the

plateau of $\eta \approx 10^{22}$ Pa s (*10*) and a slip rate of 10 mm/yr, we obtained a depth-averaged effective shear stress on the fault system that is about 2 MPa (*SM.7*). A stress drop of around 4 MPa was estimated for the 2001 Kokoxili earthquake on the Kunlun Fault (*52*), consistent with the global median of stress drops on continental transform-fault earthquakes of 3.5 MPa (*53*). Even if earthquakes on the Kunlun fault release all the stress in the seismogenic crust, average stress levels in the inferred ductile shear-zone beneath appear to be significantly less than those in the seismogenic crust.

If we assume the ductile shear zone supports similar stresses to the seismogenic fault, and the ductile shear zone is on average about 10 km wide, consistent with observations summarized in (*6*), then the apparent effective viscosity of the shear zone is about $\sim 6 \times 10^{19}$ Pa s (*SM.7*); narrower shear zones require even lower viscosities. The low-viscosity shear zones required beneath the major active faults can arise due to localization mechanisms including shear heating (e.g. *54,55*), grain size reduction (e.g. *56*), fabric development (e.g. *57*) and fluid fluxing (e.g. *58, 59*). For weakening caused by thermal feedback, an apparent reduction in effective viscosity of the shear zone by a factor of ~250 would imply a localized temperature increase (for olivine) of ~200ºC. It is likely that weakening processes are only developed and sustained for those faults with a stable geometry that can accrue significant (tens of km) displacements. Among possible schematic rheological models of the lithosphere considered by Burgmann and Dresen (*6*), our understanding of the Tibetan strain rate field is most consistent with their "banana-split" model, in which the low strength of major fault zones limits the magnitude of lithospheric stress.

Relatively few of the Tibetan fault systems exhibit high strain rates, and there is significant variation in their apparent fault resistance, *f*. Most of the known faults on the plateau (Fig. 1) are not associated with high strain rates (Fig. 2). What mechanisms allow particular lithospheric-scale fault systems, such as the Kunlun, to be activated and sustained? One explanation is that active fault systems initially develop along pre-existing suture zones that are favorably oriented with respect to the stress field, e.g., the Kunlun fault and the Anyimaqen-Kunlun-Muztagh suture (*1*). Another possibility is that deep shear zones develop along boundaries between regions of differing rheological strength, e.g., the Altyn Tagh fault along the southeast margin of the Tarim Basin (*60*). Once established, the weakened fault systems have a major effect on the distribution of velocities and strain rates across the entire plateau, and we might expect the apparent *f* value to decrease in time as fault systems mature, increasing their offset and length. For example, our models show that although extension in southern and central Tibet is driven by the contrast in gravitational potential energy on the plateau's southeastern margin, the rates of extension and their spatial extent are strongly enhanced by the relatively weak Kunlun fault system. We suggest there is a causal link between mid-Miocene activation of the Kunlun fault (*61,62*) and the apparently synchronous onset of east–west extension on a series of rifts in south-central Tibet (*63,64*).

References

1. A. Yin, T. M. Harrison, Geologic evolution of the Himalayan-Tibetan orogen, *Annu. Rev. Earth Planet. Sci.* **28**, 211–80 (2000).

2. P. England, P. Molnar, Active deformation of Asia: From kinematics to dynamics. *Science* **278**, 647-650 (1997).

3. J. P. Avouac, P. Tapponnier, Kinematic model of active deformation in central Asia. *Geophys. Res. Lett.* **20**, 895-898 (1993).

4. W. Thatcher, Microplate model for the present-day deformation of Tibet, *J. Geophys. Res.* **112**, B01401 (2007) doi:10.1029/2005JB004244

5. L. Wang, S. Barbot, Three-dimensional kinematics of the India-Eurasia collision, *Commun. Earth Environ.* **4**:164 (2023). doi:10.1038/s43247-023-00815-4

6. R. Bürgmann and G. Dresen, Rheology of the Lower Crust and Upper Mantle: Evidence from Rock Mechanics, Geodesy, and Field Observations, *Annu. Rev. Earth Planet. Sci.* **36**, 531–567 (2008).

7. S. Bourne, P. England, B. Parsons, The motion of crustal blocks driven by flow of the lower lithosphere and implications for slip rates of continental strike-slip faults. *Nature* **391**, 655-659 (1998).

8. P. Molnar, P. Tapponnier, Cenozoic tectonics of Asia: Effects of a continental collision, *Science* **189**, 419-426 (1975).

9. P. England, J. Jackson, Uncharted seismic risk. *Nat. Geosci.* **4**, 348-349 (2011).

10. J. Fang *et al.*, The Dynamics of the India-Eurasia Collision: Faulted Viscous Continuum Models Constrained by High-Resolution Sentinel-1 InSAR and GNSS Velocities, *J. Geophys. Res. Solid Earth* **129**, e2023JB028571 (2024).

11. A. Vauchez, A. Tommasi, D. Mainprice, Faults (shear zones) in the Earth's mantle, *Tectonophysics* **558-559**, 1–27 (2012).

12. M. Kahraman, *et al.*, Crustal-scale shear zones and heterogeneous structure beneath the North Anatolian Fault Zone, Turkey, revealed by a high-density seismometer array, *Earth, Planet. Sci. Lett.* **430**, 129–139 (2015).

13. P. England, D. McKenzie, A thin viscous sheet model for continental deformation. *Geophys. J. Int.* **70**, 295-321 (1982).

14. L. M. Flesch, A. J. Haines, W. E. Holt, Dynamics of the India-Eurasia collision zone. *J. Geophys. Res. Solid Earth* **106**, 16435-16460 (2001).

15. P. C. England, G. A. Houseman, The Mechanics of the Tibetan Plateau. *Philos. Trans. Roy. Soc. A* **326**, 301-320 (1988).

16. P. Tapponnier *et al.*, Oblique stepwise rise and growth of the Tibet plateau. *Science* **294**, 1671-1677 (2001).

17. C. Kreemer, G. Blewitt, E. C. Klein, A geodetic plate motion and global strain rate model. *Geochem. Geophys. Geosyst.* **15**, 3849-3889 (2014).

18. W. Wang, X. Qiao, K. Ding, Present-day kinematics in southeastern Tibet inferred from GPS measurements. *J. Geophys. Res. Solid Earth* **126**, e2020JB021305 (2021).

19. M. Wang, Z.-K. Shen, Present-Day Crustal Deformation of Continental China Derived From GPS and Its Tectonic Implications. *J. Geophys. Res. Solid Earth* **125**, e2019JB018774 (2020).

20. E. Attema *et al.*, Sentinel-1 ESA's new European radar observatory. *EUSAR 2008*, (2008).

21. M. Lazecký *et al.*, LiCSAR: An automatic InSAR tool for measuring and monitoring tectonic and volcanic activity. *Remote Sens.* **12**, 2430 (2020).

22. Y. Morishita *et al.*, LiCSBAS: An Open-Source InSAR Time Series Analysis Package Integrated with the LiCSAR Automated Sentinel-1 InSAR Processor. *Remote Sens.* **12**, 424 (2020).

23. W.-P. Ge, P. Molnar, Z.-K. Shen, and Q. Li, Present-day crustal thinning in the southern and northern Tibetan Plateau revealed by GPS measurements, *Geophys. Res. Lett.* **42**, 5227–5235 (2015) doi:10.1002/2015GL064347.

24. P. Molnar, P. England, J. Martinod, Mantle dynamics, the uplift of the Tibetan Plateau and the Indian Monsoon, *Rev. Geophys.* **31**, 357-396 (1993).

25. M. Lazecky *et al.*, LiCSAR Extra & LiCSBAS. Zenodo. https://doi.org/10.5281/zenodo.17734804 (2025).

26. H. Wang, T.J. Wright, Satellite geodetic imaging reveals high strain away from major faults of Western Tibet. *Geophys. Res. Lett.* **39**, L07303 (2012).

27. Wang, H., Wright, T. J., velmap (v1.1). Zenodo. https://doi.org/10.5281/zenodo.17713962 (2025).

28. J. R. Weiss *et al.*, High-Resolution Surface Velocities and Strain for Anatolia From Sentinel-1 InSAR and GNSS Data. *Geophys. Res. Lett.* **47**, e2020GL087376 (2020).

29. G. Zheng *et al.*, Crustal deformation in the India-Eurasia collision zone from 25 years of GPS measurements. *J. Geophys. Res. Solid Earth* **122**, 9290-9312 (2017).

30. Q. Ou *et al.*, Large-Scale Interseismic Strain Mapping of the NE Tibetan Plateau From Sentinel-1 Interferometry. *J. Geophys. Res. Solid Earth* **127**, e2022JB024176 (2022).

31. H. Ansari, F. De Zan, A. Parizzi, Study of systematic bias in measuring surface

deformation with SAR interferometry. *IEEE Trans. Geosci. Remote Sens.* **59**, 1285-1301 (2020).

32. R. Grandin *et al.*, Long-term growth of the Himalaya inferred from interseismic InSAR measurement. *Geology*, **40**(12), 1059-1062 (2012).

33. Q. Zhao *et al.*, The vertical velocity field of the Tibetan Plateau and its surrounding areas derived from GPS and surface mass loading models. *Earth and Planetary Science Letters*, **609**, p.118107 (2023).

34. S. Liu, S. Jónsson., Glacial isostatic uplift in the Tibetan Plateau and surroundings. *Geophysical Research Letters* **52** (13), e2025GL114899 (2025).

35. G.A. Houseman, P.C. England, L.A. Evans, L.A., Gravitational instability of thickened yet compositionally buoyant Tibetan mantle lithosphere. *Tectonophysics*, **911**, p.230837 (2025).

36. Y. Chen, M. Liu, Correlation between Strain Rate and Seismicity in Different Tectonic Settings, *Seismol. Res. Lett.* **95**, 2375–2385 (2024). doi: 10.1785/0220230306

37. W.-J. Zheng *et al.*, Late Quaternary slip rate of the South Heli Shan Fault (northern Hexi Corridor, NW China) and its implications for northeastward growth of the Tibetan Plateau. *Tectonics* **32**, 271-293 (2013).

38. J. Guo *et al.*, Surface ruptures associated with the 1937 M 7.5 Tuosuo Lake and the 1963 M 7.0 Alake Lake earthquakes and the paleoseismicity along the Tuosuo Lake segment of the Kunlun Fault, Northern Tibet. *Bull. Seismol. Soc. Am.* **97**(2), 474-496 (2007).

39. T.J. Wright, 2016. The earthquake deformation cycle. *Astronomy and Geophysics* **54**(7), 4-20.

40. E. Hussain *et al.*, Constant strain accumulation rate between major earthquakes on the North Anatolian Fault. *Nat. Commun.* **9**, 1392 (2018).

41. T. Yamasaki, T. J. Wright, G. A. Houseman, Weak ductile shear zone beneath a major strike-slip fault: Inferences from earthquake cycle model constrained by geodetic observations of the western North Anatolian Fault Zone. *J. Geophys. Res. Solid Earth* **119**, 3678-3699 (2014).

42. B. Meade, Y. Klinger, E.A. Hetland, Inference of multiple earthquake-cycle relaxation timescales from irregular geodetic sampling of interseismic deformation. *Bull. Seismol. Soc. Am.* **103**, 2824-2835 (2013). doi:10.1785/0120130006

43. G.A. Houseman, basil (v1.7.6a). Zenodo. https://doi.org/10.5281/zenodo.10052242 (2023).

44. G. Hirth, D. Kohlstedt, Rheology of the upper mantle and the mantle wedge: A view from the experimentalists. In: Eiler, J. (Ed.), Inside the Subduction Factory, American Geophysical Union (2013).

388   45.   L.J. Sonder, P.C. England, Vertical averages of rheology of the continental lithosphere;
389   relation to thin sheet parameters, *Earth Planet. Sci. Lett.* **77**, 81–90 (1986).

390   46.   C. DeMets, S. Merkouriev, S. Jade, High-resolution reconstructions and GPS estimates of
391   India–Eurasia and India–Somalia plate motions: 20 Ma to the present. *Geophys. J. Int.*
392   **220**, 1149-1171 (2020).

393   47.   C. DeMets, R.G. Gordon, D.F. Argus, Geologically current plate motions. *Geophys. J.*
394   *Int.* **181**(1), 1–80 (2010).

395   48.   C. Amante, B.W. Eakins, ETOPO1 arc-minute global relief model: procedures, data
396   sources and analysis. (2009).

397   49.   S.M. Chung *et al.*, Tibetan tectonic evolution inferred from spatial and temporal variations
398   in post-collisional magmatism, *Earth-Science Reviews,* 68, 173 – 196
399   doi:10.1016/j.earscirev.2004.05.001 (2005).

400   50.   L. Ding, P. Kapp, D. Zhong and W. Deng. Cenozoic Volcanism in Tibet: Evidence for
401   Transition from Oceanic to Continental Subduction, *J. Petrology*, 44, 1833-1865 (2003).
402   10.1093/petrology/egg061

403   51.   S.L. Klemperer. Crustal flow in Tibet: geophysical evidence for the physical state of
404   Tibetan lithosphere, and inferred patterns of active flow, *in*: Law, R.D., M.P. Searle and
405   L. Godin,(eds.) Channel Flow, Ductile Extrusion and Exhumation in Continental
406   Collision Zones. *Geological Society, London, Special Publications*, 268, 39–70 (2006).

407   52.   M. Antolik, R.E.Abercrombie, G. Ekstrom, The 14 November 2001 Kokoxili (Kunlun
408   Shan), Tibet, Earthquake: Rupture transfer through a large extensional step-over, *Bull.*
409   *Seismol. Soc. Am.* **94**, 1173–1194 (2004). https://doi.org/10.1785/012003180

410   53.   B.P.Allmann, P.M. Shearer, Global variations of stress drop for moderate to large
411   earthquakes, *J. Geophys. Res.* **114** (B1) (2009). doi:10.1029/2008JB005821

412   54.   C.S.Takeuchi, Y. Fialko, Dynamic models of interseismic deformation and stress transfer
413   from plate motion to continental transform faults. *J. Geophys. Res.* **117**, B05403, (2012).
414   doi:10.1029/2011JB009056

415   55.   K. Willis*, et al.*, Strain localization by shear heating and the development of lithospheric
416   shear zones, *Tectonophysics* **764**, 62–76 (2019).

417   56.   J.H.P. De Bresser, J.H. Ter Heege, C.J. Spiers, Grain size reduction by dynamic
418   recrystallization: can it result in major rheological weakening? *Int. J. Earth Sci.* **90**, 28-45
419   (2001). doi:10.1007/s005310000149

420   57.   L.G.J. Montési, Fabric development as the key for forming ductile shear zones and
421   enabling plate tectonics, *J. Struct. Geol.* (2013). doi:10.1016/j.jsg.2012.12.011

422   58.   J.A. Jackson, H. Austrheim, D. McKenzie, K. Priestley, Metastability, mechanical
423   strength, and the support of mountain belts, *Geology* **32**, 625–628 (2004)

424   doi:10.1130/G20397.1

59.   M. Carpenter, S. Piazolo, T. Craig, T. Wright, Mid-crustal strain localisation triggered by localised fluid influx and activation of dissolution-precipitation creep, *J. Struct. Geol.* **199**, 105461, doi: 10.1016/j.jsg.2025.105461 (2025)

60.   K.E. Dayem, G.A. Houseman, P. Molnar, Localization of shear along a lithospheric strength discontinuity: Application of a continuous deformation model to the boundary between Tibet and the Tarim Basin, *Tectonics* **28**, TC3002, (2009) doi:10.1029/2008TC002264

61.   A.R. Duvall *et al.*, Low-temperature thermochronometry along the Kunlun and Haiyuan Faults, NE Tibetan Plateau: Evidence for kinematic change during late-stage orogenesis, *Tectonics* **32**, 1190–1211 (2013).

62.   L.M. Staisch, N.A. Niemi, M.K. Clark, H. Chang, The Cenozoic evolution of crustal shortening and left-lateral shear in the central East Kunlun Shan: Implications for the uplift history of the Tibetan Plateau. *Tectonics* **39**, e2020TC006065 (2020).

63.   J. Lee *et al.*, Middle to late Miocene extremely rapid exhumation and thermal re-equilibration in the Kung Co rift, southern Tibet, *Tectonics* **30**, TC2007 (2011).

64.   R.H. Styron *et al.*, Miocene initiation and acceleration of extension in the South Lunggar rift, western Tibet: Evolution of an active detachment system from structural mapping and (U-Th)/He thermochronology, *Tectonics* **32**, 880–907 (2013).

65.   T.J. Wright *et al*., Deformation, Strains, and Velocities for the Tibetan Plateau from Sentinel-1 InSAR, GNSS, and Levelling Data, version 1. *NERC EDS Centre for Environmental Data Analysis*, https://catalogue.ceda.ac.uk/uuid/6181ff81c7dc4ab2a492c8f53f58df52/, doi:10.5285/6181ff81c7dc4ab2a492c8f53f58df52 (2025).

66.   R. Styron, M. Pagani, The GEM global active faults database. *Earthq. Spectra* **36**, 160-180 (2020).

67.   T.J. Wright, B. Parsons, Z. Lu, Toward mapping surface deformation in three dimensions using InSAR. *Geophys. Res. Lett.* **31** (2004)

68.   P. England, G.A. Houseman, L.Sonder, Length scales for continental deformation in convergent, divergent, and strike-slip environments: Analytic and approximate solutions for a thin viscous sheet model, *J. Geophys. Res. Solid Earth* **90**, 3551-3557 (1985).

69.   Yu, C., Li, Z., Penna, N. T., Crippa, P., Generic atmospheric correction model for interferometric synthetic aperture radar observations, *J. Geophys. Res. Solid Earth* **123**(10), 9202-9222 (2018).

70.   Z. Yunjun, Fattahi, H., Pi, X., Rosen, P., Simons, M., Agram, P., Aoki, Y., Range geolocation accuracy of C-/L-band SAR and its implications for operational stack coregistration. *IEEE Trans. Geosci. Remote Sens.* **60**, 1-19 (2022).

71. X. Xu, Sandwell, D. T., Toward absolute phase change recovery with InSAR: Correcting for earth tides and phase unwrapping ambiguities. *IEEE Trans. Geosci. Remote Sens.* **58**(1), 726-733 (2019).

72. P. Wessel, Luis, J. F., Uieda, L. A., Scharroo, R., Wobbe, F., Smith, W. H., Tian, D., The generic mapping tools version 6. *Geochem. Geophys. Geosyst.* **20**(11), 5556-5564 (2019).

73. M. Lazecky, Fang, J., Hooper, A., Wright, T., Improved phase unwrapping algorithm based on standard methods. In *IGARSS 2022-2022 IEEE International Geoscience and Remote Sensing Symposium* (pp. 743-746). IEEE (2022).

74. O. L. Stephenson, *et al.*, The impact of plate motions on long-wavelength InSAR-derived velocity fields. *Geophys. Res. Lett.* **49**(21), e2022GL099835 (2022).

75. J. Elliott *et al.*, Deformation, Strains and Velocities for the Alpine Himalayan Belt from trans-continental Sentinel-1 InSAR & GNSS. EarthArXiv eprints (2025): https://doi.org/10.31223/X5GX6B.

76. Z. Altamimi, *et al.*, ITRF2014 plate motion model. *Geophys. J. Int.* **209**, 1906–1912 (2017).

77. A. Love, A treatise on the mathematical theory of elasticity. Courier Corporation, (1944).

78. J. Fang *et al.*, Strain partitioning in the Southeastern Tibetan Plateau from kinematic modeling of high-resolution Sentinel-1 InSAR and GNSS. Geophysical Research Letters, **51**(19), 2024GL111199 (2024).

Author contributions:

497   Conceptualization: TJW, GAH, JF, BP

498   Methodology: TJW, GAH, JF, YM, AJH, LE, ML, QO, CR, HW, DW

499   Investigation: TJW, GAH, JF, YM, DW

500   Visualization: TJW, GAH, JF

501   Funding acquisition: TJW, BP, JRE

502   Writing – original draft: TJW, GAH

503   Writing – review & editing: All

504   **Competing interests:** Authors declare that they have no competing interests.

505   **Data and materials availability:** GNSS and levelling data, LOS velocities, LiCSBAS
506   processing parameters, 3D velocity grids, strain rates and *velmap* outputs created and used in
507   this study are available in CEDA repository:
508   doi:10.5285/6181ff81c7dc4ab2a492c8f53f58df52 (*65*). All other data needed to evaluate the
509   conclusions in the paper are present in the paper or the supplementary materials. No new
510   physical materials were generated for this study.

511

512   SUPPLEMENTARY MATERIALS

513   Materials and Methods

514   Figs. S1 to S19

515   References (*67-78*)
516
517
518
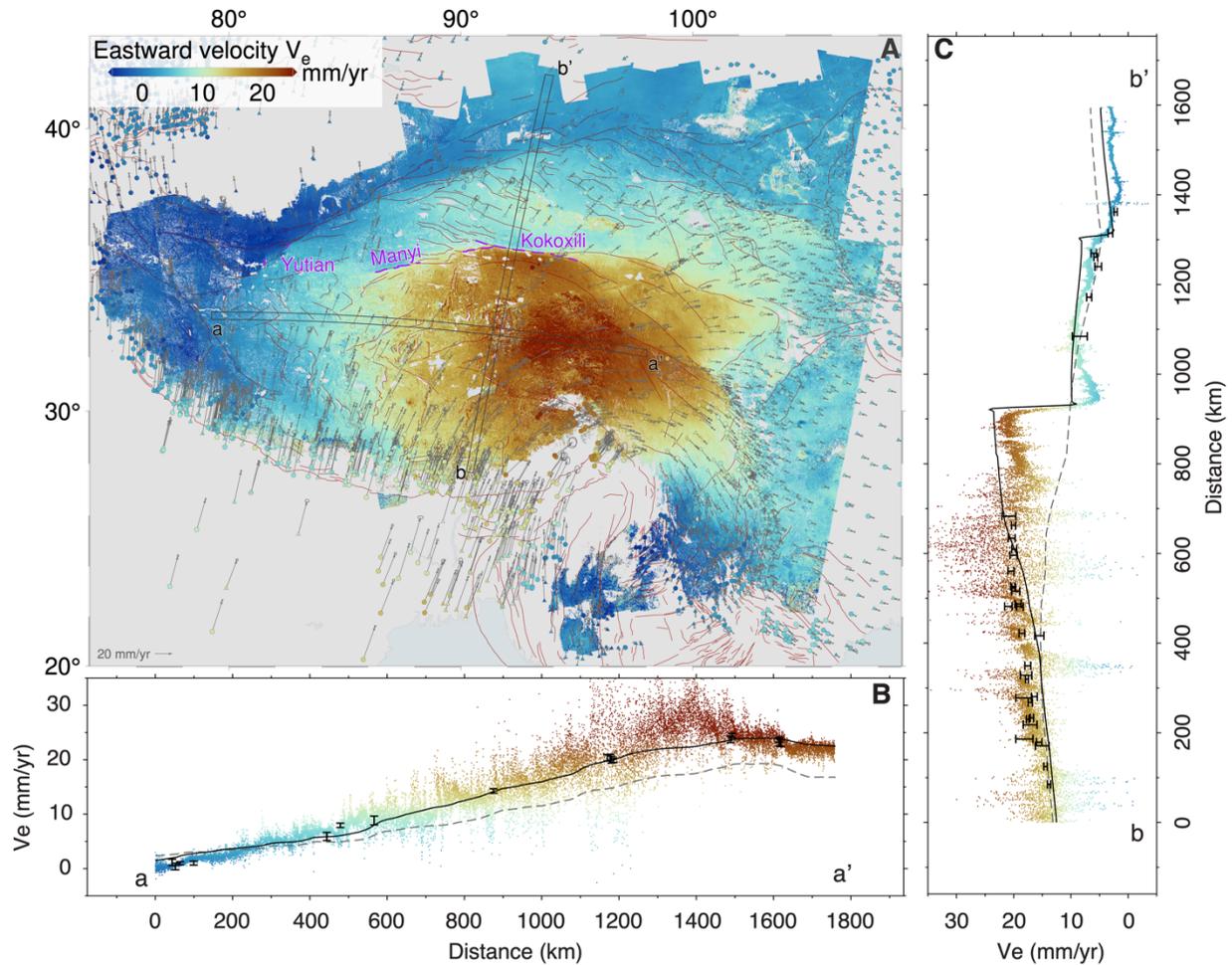
Fig. 1. High-resolution velocity field of Tibet. (A) East component of the velocity field for Tibet derived from the geo-referenced InSAR, overlain with velocity vectors from GNSS observation points marked by colored circles (2D sites) and triangles (3D) (*SM.4*), relative to a fixed Eurasia reference frame. Faults, shown as dark red lines, are from the Global Earthquake Model (*66*), with purple dashed lines indicating the ruptures of the 1997 Manyi and 2001 Kokoxili earthquakes, associated with the Kunlun fault zone, and 2008 and 2014 Yutian earthquakes, associated with the Altyn Tagh fault zone (Fig. 2C). (B), (C) profiles of the eastward velocity component along lines marked a-a' and b-b' in (A). Colored dots are east velocities from the InSAR grid within 15 km of the profile line; black bars show GNSS east velocities within 100 km of the profile and their formal uncertainties (±1 standard deviation; *SM.4*); the solid black line is the prediction of our best-fit geodynamic model (*SM.7*); the gray dashed line is the best geodynamic model we obtained without including faults.
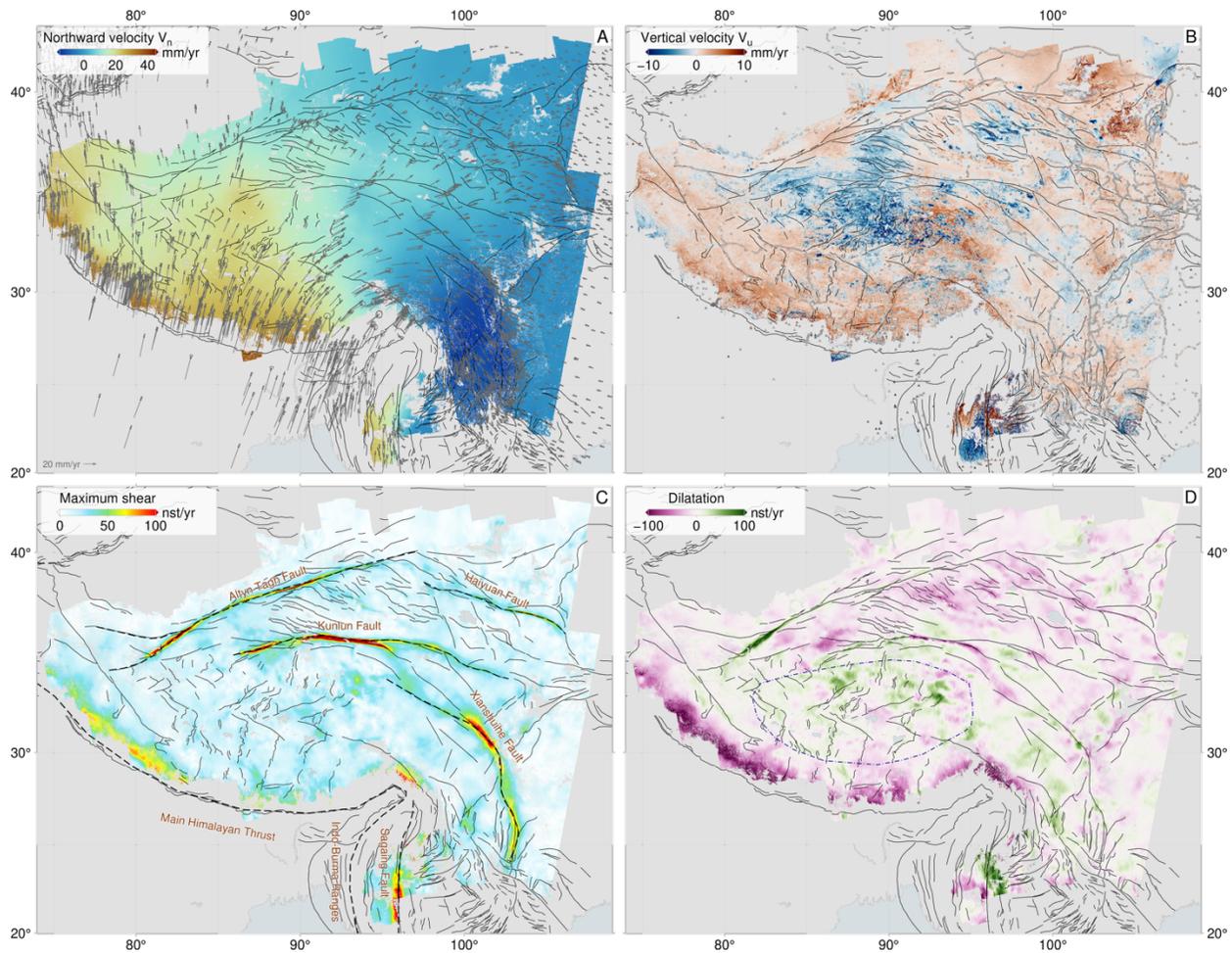
Fig. 2. Components of the estimated horizontal strain rate field. (A) Northward velocity field from the *coarse* velocity model, overlain with GNSS horizontal velocity vectors. (B) High-resolution vertical velocity field derived from geo-referenced InSAR, constrained by vertical GNSS measurements (colored triangles) and levelling data (circles) (Fig. S2). (C) Maximum shear strain rate (nanostrain/yr) and (D) horizontal dilatation rate (green=expanding; purple=contracting) derived from gradients of the InSAR data (*SM.5*). Thick dashed black lines in (C) show the major faults we include in our geodynamic model; thin black lines are from the Global Earthquake Model (*66*). The dotted blue region in (D) defines the area used for calculating average strain rate cited in the text.
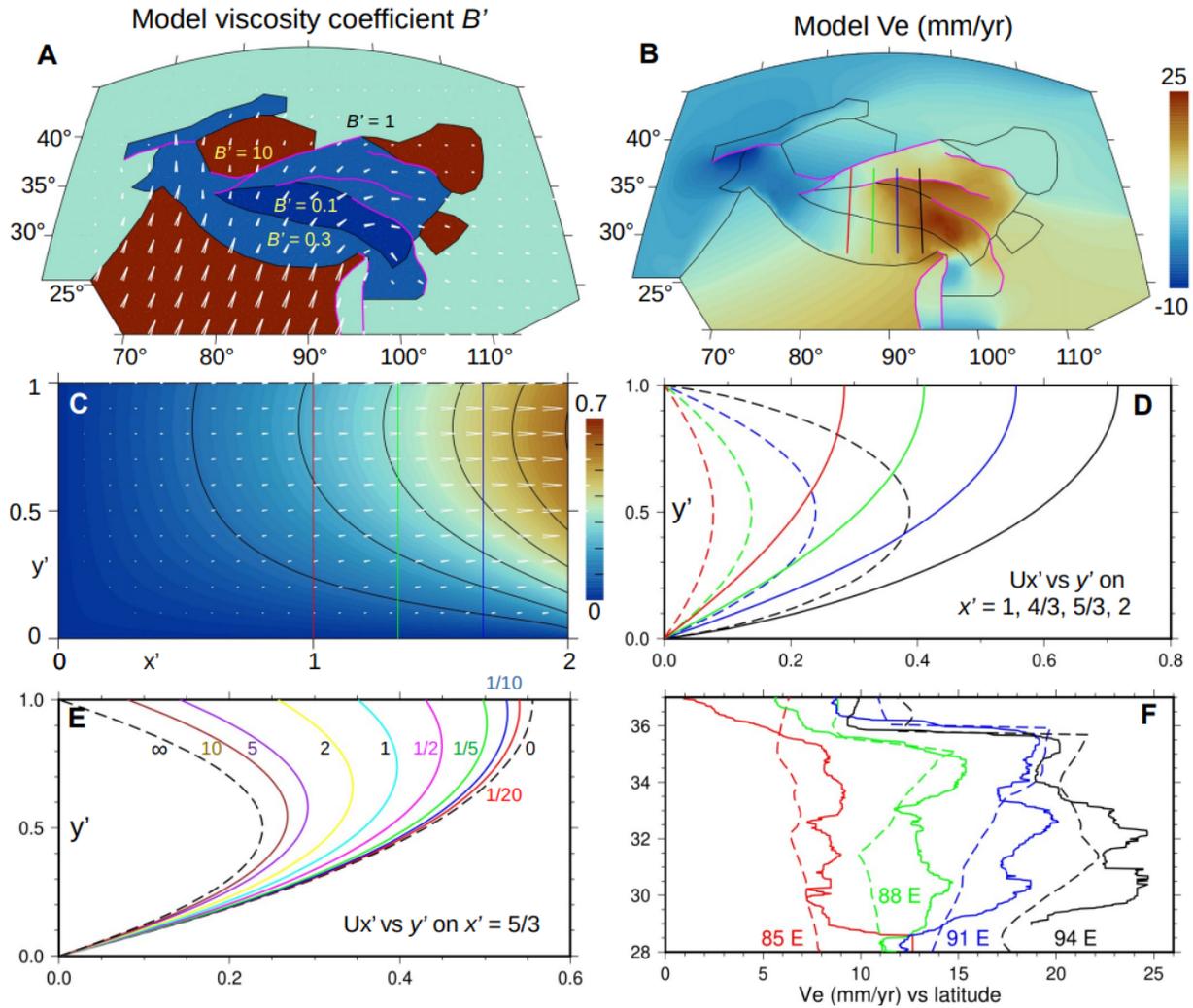
Fig. 3. Comparison of observed and modelled eastward velocity fields. (A) Regional variation of viscosity coefficient used in the preferred thin viscous shell model (*10*); black lines represent regional boundaries and magenta lines are model faults; the model velocity field is indicated by white arrows; (B) East component of the model velocity field V_e (mm/yr), for comparison with observed V_e (Fig. 1), (C) Simplified conceptual model showing velocity in the x' direction, $U_{x'}$, within a uniform rectangular region $0 \leq x' \leq 2; 0 \leq y' \leq 1$ with outflow on $x' = 2$ driven by a step in gravitational potential energy, and boundary $y' = 1$ representing a fault with resistance coefficient $f' = 0.5$, (D) y-direction profiles of $U_{x'}$ on $x' = 1, 4/3, 5/3, 2$ of the simplified model for $f' = 0$ (solid lines) and $f' = $ infinity (dashed lines), (E) y-direction profiles to show effect on $U_{x'}$ at $x' = 5/3$, of the boundary f' varied between 0 and ∞. (F) scaled profiles of observed V_e (solid lines) compared to V_e computed from thin viscous shell model (dashed lines) at constant longitude profiles marked on (B).

Science

AAAS

Supplementary Materials for

High-resolution geodetic velocities reveal role of weak faults in deformation of Tibetan Plateau

Authors: T.J. Wright[1]*, G.A. Houseman[2,1], J. Fang[1]*, Y. Maghsoudi[3], A.J. Hooper[1], J.R. Elliott[1], L. Evans[4], M. Lazecky[1], Q. Ou[5], B.E. Parsons[6], J.C. Rollins[7], L. Shen[8], H. Wang[9], D. Wang[1]

Affiliations:
[1] COMET, School of Earth and Environment, University of Leeds, Leeds, UK
[2] State Key Laboratory of Deep Earth Exploration and Imaging, China University of Geosciences, Beijing, China
[3] COMET, Department of Earth and Environmental Sciences, University of Exeter, Penryn, UK
[4] School of Earth, Atmosphere & Environment, Monash University, Clayton, VIC, Australia
[5] COMET, School of GeoSciences, University of Edinburgh, Drummond, Edinburgh, UK
[6] COMET, Department of Earth Sciences, University of Oxford; Oxford, UK
[7] GNS Science, Lower Hutt, New Zealand
[8] Lamont-Doherty Earth Observatory, Columbia University, New York, USA
[9] College of Natural Resources and Environment, South China Agricultural University, Guangzhou, China

*Corresponding author. Email: t.j.wright@leeds.ac.uk (T.J.W.); j.fang@leeds.ac.uk (J.F.)

This PDF file includes:

Materials and Methods

1. InSAR processing

We processed data from ~44,500 Sentinel-1 SAR acquisitions to create ~341,400 interferograms using the COMET-LiCSAR system (*21*). This system was built to automatically create Sentinel-1 interferograms from 250-km-wide Interferometric Wide Swath data acquired over the continents. We divide that land surface up into 127 ascending and 114 descending frames that are typically 250 km long, and process interferometric networks in short-baseline configurations, typically aiming to connect each epoch to the closest 4 epochs in time, adding in 6-month and 12-month interferograms to minimize the impact of phase bias. In Tibet, most data were acquired with a 12-day revisit. We define some frames to be larger than the 250 km standard definition, typically where frame boundaries coincide with major faults, or where boundaries needed to be adjusted to coincide with a switch from Sentinel-1A to -1B. All interferograms are available in Geotiff format via the COMET-LiCSAR portal (https://comet.nerc.ac.uk/comet-lics-portal/) and via the CEDA archive (https://data.ceda.ac.uk/neodc/comet/data/licsar_products). Individual networks used for time series analysis in each frame are also available via the CEDA archive (*66*).

2. Estimating average line-of-sight velocities

We correct the LiCSAR data for modeled troposphere (*69*), ionosphere (*70*) and earth tides (*71, 72*), and down-sample during an updated unwrapping procedure (*73*) from ~100 m to ~1 km resolution. We calculate average line-of-sight velocities for each LiCSAR frame using the LiCSBAS code *(22,25)*, which finds the best fit long-term velocity on a pixel-by-pixel basis, using the available short-baseline network. The approach accounts for any gaps in the network and identifies and removes unwrapping errors found by checking closure phase around triangular loops. We additionally performed a careful visual inspection to remove all the remaining poor-quality interferograms prior to the LiCSBAS inversion. After the inversion, we masked noisy pixels using noise indices, including the number of unclosed loops and the RMS of residuals in the small baseline inversion; we adjusted these parameters for each frame to optimize the results. We further flattened the bootstrapping-derived velocity standard deviation, using semi-variogram analysis to remove the impact of distance from the reference area (*30*). Additionally, we estimated and subtracted the motion of the Eurasian plate from all frames (*74*). Some of the key processing parameters are listed at (*66*).

The line-of-sight velocities for all the frames used in this analysis are available to download from the CEDA archive (*66*).

3. Correcting for earthquakes

To correct for earthquakes that occurred in the time period of the observations, we solve for a step in the line-of-sight displacements and use the average line-of-sight velocities excluding the coseismic displacements. We apply this correction to earthquakes larger than M6. The exception is M_w 7.3 Maduo Earthquake in Southern Qinghai, China, which was the only earthquake larger than M_w 7 that occurred in our observation period. For the frames impacted by this earthquake, we truncate the time series and only present the inter-seismic velocities measured before the earthquake. Details of any earthquake corrections applied to individual frames are provided on the CEDA archive (*66*).

4. GNSS and levelling compilation

87 We compile 18,203 GNSS velocities and 6,607 levelling rates (plus 4 SLR, 2 DORIS and 2 VLBI
88 velocities) in the vicinity of the Tibetan Plateau (73.5 to 112ºE and 20 to 45ºN) from 131 studies and
89 datasets published since 2013 (data and studies listed at *66*). We prepare and combine these velocities
90 in a multi-step procedure summarized below. More details are provided in *(75)*.

91 1. First, we transform each input dataset into the ITRF2014 Eurasia-fixed reference frame *(76)*.

92 2. Next, we improve the precision of some GNSS velocities whose locations are rounded to the
93   nearest 0.1° or 0.01°, by linking velocities in different datasets that are at the same site and
94   using the highest-precision location available for each linked site.

95 3. We identify 14 velocities that do not have uncertainties provided but do have site occupation
96   durations and numbers of occupations evident, and we use these metadata to estimate the
97   velocity uncertainties with a model that combines random-walk, white and flicker noise. We
98   also round up unrealistically small positive uncertainties to a minimum of 0.05 mm/yr for the
99   east and north components (the 2.275th-percentile or -2σ value of all compiled east and north
100   uncertainties) and 0.12 mm/yr for the vertical component (the -2σ value of compiled vertical
101   uncertainties). This rounding is applied to 129 east, 108 north and 107 vertical uncertainties.

102 4. We then begin flagging and removing outlier velocities. We first flag 71 velocities that have site
103   occupation times of <1.5 yr, east or north uncertainties of >5 mm/yr (the $+3\sigma$ value of the
104   compiled east and north uncertainties), vertical uncertainties of >24 mm/yr (the $+3\sigma$ value of
105   compiled vertical uncertainties), or uncertainties that are zero or remain undefined.

106 5. We then use an iterative automated approach to flag other outlier velocities. For each velocity in
107   the dataset, we find the population of velocities at nearby sites and compute a central value
108   (halfway between the median and mean) and mean absolute deviation (MAD) of that
109   population's velocities in both the east and north components. We flag outliers as velocities that
110   deviate from the central value by more than a scalar multiple of the MAD (in either the east or
111   north component). The multiple of the MAD is started at a relatively high value to detect the
112   most obvious outliers first (and exclude them from the nearby population in subsequent
113   iterations), then iteratively brought down to a final preferred value of 3.75. This flags 432
114   outliers in total, which are then removed.

115 6. Next, we use another iterative method to remove remaining systematic velocity differences
116   between datasets (arising from their uses of different stations to get into their original reference
117   frames). For each study or dataset, we tabulate the differences between that study's velocities
118   and all other studies' velocities at any common sites, fit those differences to an Euler-pole
119   rotation using least squares, and apply 1/20 (5%) of that rotation to that study, then move on to
120   the next study. After proceeding through all of the studies, we recalculate all of the velocity
121   differences and run another iteration. This is done for 200 total iterations (100 in which
122   compilation studies such as *(19)* are treated as single studies, and a second 100 in which they
123   are split out into their constituent studies, by which time the rotations being applied are
124   extremely small).

3

125   7. After alignment, we reapply the automatic outlier detector to identify and remove 90 other
126   outliers that become apparent in the aligned field. We also remove 1,886 velocities that are
127   based entirely on data preceding the Sentinel-1 era (2014-present) and are superseded by newer,
128   high-quality measurements at the same locations, plus 1,349 other duplicate velocities. This
129   leaves 14,373 GNSS velocities.

130   8. Finally, we combine collocated GNSS velocities by (for each component) computing a central
131   value that lies halfway between the mean and the median of the velocities being combined. We
132   compute several alternate measures of uncertainty on this central value, exploring three "meta-
133   uncertainties": whether to take into account the uncertainties on the velocities being combined,
134   whether to treat different studies' velocities at the same site as independent data or not, and
135   whether to use the standard deviation or the mean absolute deviation as the measure of spread.
136   These three different either-or options imply eight different metrics of uncertainty on the mean
137   velocity and a separate eight for the median, or 64 different possible uncertainty metrics on the
138   average of the mean and median. We compute the combined uncertainty that would result from
139   each of these 64 different metrics, then take the average of the mean and median of those 64 as
140   the final uncertainty (for each component, at each station with multiple velocities).

141 For purposes of our modelling, we also discard vertical velocities with absolute values exceeding 20
142 mm/yr from the final combined dataset; however, these may be useful for other studies of nontectonic
143 processes. The final combined point-velocity dataset (available at *66*) includes 3142 horizontal
144 velocities (from 1707 2D and 1435 3D GNSS sites) and 7767 vertical rates (from 1435 3D and 70 pure
145 vertical GNSS, as well as 6262 levelling rates) in the study region (Fig. S2).

146 The GNSS data format columns are as follows:

147 2D dataset: longitude; latitude; eastward and northward velocities; 1-sigma uncertainties in the
148 eastward and northward components; east-north covariance (assumed zero); station type (GNSS);
149 station name; study identifier.

150 3D dataset: longitude; latitude; eastward, northward, and vertical velocities; 1-sigma uncertainties in
151 the eastward, northward, and vertical components; the three velocity covariances (all assumed zero);
152 station type (GNSS or levelling); station name; study identifier.

153 For purely vertical GNSS and levelling data, horizontal velocities are assumed zero with a large
154 uncertainty of 1,000,000 mm/yr.

155 GNSS stations and the plotted profiles in Fig. 1B,1C can be extracted from the GNSS data file with the
156 following command using the generic mapping tools software (*72*):

157 gmt project $gnssfile -C79.25/33.51 -E98.02/32.14 -Q -Lw -Fxypz -W-50/50 > gnss_prof_a.txt

158 gmt project $gnssfile -C90.38/27.67 -E93.82/41.75 -Q -Lw -Fxypz -W-50/50 > gnss_prof_b.txt

159
160 <u>5. Velocity field generation</u>

161

162 To create a unified, coarse velocity field that fits the GNSS, levelling and InSAR data, and which we
163 will refer to as the *coarse* velocity model, we follow the procedure developed by *(26)*. We first
164 establish a triangular mesh covering the region of interest, using a set of nodes spaced by ~0.20 degrees
165 in longitude and latitude (Fig. S1). We then use the *velmap* code *(27)* to invert simultaneously for the
166 best-fit 3D velocities at each node (Fig. S3), reference frame adjustment parameters for each InSAR
167 frame, and a linear-with-height atmospheric correction term for each frame. The reference frame
168 adjustment parameters consist of a second-order polynomial surface. Before inverting for the velocity
169 field, InSAR data are downsampled to 5 km resolution.

170

171 As described in *(26)*, velocities at observation points (in the InSAR and GNSS) are linked to the
172 velocities at the nodes of the mesh using linear interpolation functions, which account for variations in
173 the satellite line of sight, and we minimize the weighted square misfit between the observations and
174 predictions. Regularization is applied using Laplacian smoothing to ensure a physically meaningful
175 solution and to handle data gaps.

176

177 The derived reference frame adjustment parameters enable us to create mosaics of ascending and
178 descending line-of-sight velocities in a Eurasia reference frame, at the 1 km resolution, and including
179 the linear-with-height atmospheric correction (Fig. S4). We can then invert pixel-by-pixel for the east-
180 west (Fig. 1) and vertical velocities (Fig. S5) directly from the referenced line-of-sight velocities, using
181 the north-south velocities from the *coarse* 3D velocity model (Fig. S3a) as a constraint; InSAR has
182 minimal sensitivity to the north-south velocities, but any error in the north-south velocity field will
183 propagate into an error in the vertical velocities *(67)*.

184

185 We calculate strain and rotation rates (Figs. 2, S6,S7) by first taking the horizontal gradients of both the
186 east-west velocities at InSAR resolution (Fig.1) and the north-south velocities derived from the *coarse*
187 velocity model (Fig. S3a). We derive the second invariant ($\dot{\varepsilon}_{II_h}$), maximum shear ($\dot{\varepsilon}_{shear}$), dilatation
188 ($\dot{\varepsilon}_{dil}$), and vorticity ($\dot{\omega}$) components of the horizontal strain rate tensor ($\dot{\varepsilon}_h$), as defined in Equations
189 S1-S5 (which include the spherical correction terms; *77*). To match the spatial resolution in both
190 directions, which minimizes on-fault strain artefacts arising from having different resolutions (e.g. Fig.
191 S14 in *78*), we apply a 150 km median smoothing filter to the east-west velocities with parameters
192 chosen to optimize the tradeoff between spatial resolution and noise (Fig. S8).

193

$$\dot{\varepsilon}_h = \begin{bmatrix} \dot{\varepsilon}_{xx} & \dot{\varepsilon}_{xy} \\ \dot{\varepsilon}_{yx} & \dot{\varepsilon}_{yy} \end{bmatrix} = \begin{bmatrix} \dfrac{\partial V_E}{\partial x} - \dfrac{V_N \cos\theta}{r \sin\theta} & -\dfrac{1}{2}\left(\dfrac{\partial V_E}{\partial y} + \dfrac{\partial V_N}{\partial x} + \dfrac{V_E \cos\theta}{r \sin\theta} \right) \\ -\dfrac{1}{2}\left(\dfrac{\partial V_N}{\partial x} + \dfrac{\partial V_E}{\partial y} + \dfrac{V_E \cos\theta}{r \sin\theta} \right) & \dfrac{\partial V_N}{\partial y} \end{bmatrix} \tag{S1}$$

$$\dot{\varepsilon}_{II_h} = \sqrt{\dot{\varepsilon}_{xx}^2 + 2\dot{\varepsilon}_{xy}^2 + \dot{\varepsilon}_{yy}^2} \tag{S2}$$

$$\dot{\varepsilon}_{shear} = \sqrt{\dot{\varepsilon}_{xy}^2 + \frac{(\dot{\varepsilon}_{xx} - \dot{\varepsilon}_{yy})^2}{4}} \tag{S3}$$

$$\dot{\varepsilon}_{dil} = \dot{\varepsilon}_{xx} + \dot{\varepsilon}_{yy} \tag{S4}$$

$$\dot{\omega} = \frac{\partial V_N}{\partial x} - \frac{\partial V_E}{\partial y} \tag{S5}$$

194 where V_E and V_N are the eastward and northward velocities, respectively, θ is the colatitude of each
195 pixel, and r is the Earth's radius (r=6378 km).

5

196
197   6. Data weighting and uncertainty estimation
198
199   We weight data sets using the uncertainties for the GNSS/levelling velocities (*SM.4*) and the
200   uncertainty in the line-of-sight velocities estimated (pixel-by-pixel) by LiCSBAS *(22,25)*. We
201   downsample InSAR data to 5 km before carrying out the velocity field inversion, and we include
202   spatial covariances in the InSAR data in the inversion.
203
204   We exploit the fact that we have redundant and independent InSAR observations in many locations,
205   due to overlapping tracks, to obtain an informal estimate of the uncertainties in the Eurasian-referenced
206   InSAR and in the high-resolution (pixel by pixel) east-west and vertical velocities. For pixels where we
207   have 4 independent observations of line-of-sight velocity (2 ascending tracks and 2 descending tracks),
208   we can calculate 4 estimates of the east-west and vertical velocities, each using data from a single
209   ascending and single descending track (i.e. A1+D1; A1+D2; A2+D1; A2+D2). From these, we can
210   make 2 sets of maps that show the differences between inversions that use independent InSAR data (i.e.
211   A1+D1 vs A2+D2, A1+D2 vs A2+D1). These differences have standard deviations of 2.2 and 2.1
212   mm/yr in east-west and 1.8 and 1.9 mm/yr in vertical (Fig. S9). If we assume that these differences
213   result from noise that is split equally between the independent estimates, and that the uncertainties have
214   zero mean, we can relate the variance in the difference grid to the uncertainties in each of the
215   independent inversions. This gives uncertainties in east-west and vertical velocities for pixels where
216   only two data sets exist of ~1.5 and ~1.3 mm/yr, respectively. This approach ignores any systematic
217   long-wavelength uncertainty that might arise from the GNSS data, which is common to all inversions.
218
219   For pixels where three line-of-sight data sets exist (*i.e.*, 2 ascending + 1 descending; 1 ascending +2
220   descending), we can exclude one of the redundant data sets and calculate the standard deviation of the
221   difference between the velocity of the excluded data set, Vel_r, and the line-of-sight velocity predicted
222   for that excluded geometry from the eastward and vertical field generated with the remaining two data,
223   Vel_p. These are 2.5 mm/yr when excluding data from an ascending track and 2.3 mm/yr when
224   excluding data from a descending track (Fig. S10). We can calculate the uncertainty on Vel_p as
225

$$\sigma_{Vel_p} = \sqrt{\left(los_e \sigma_{v_e}\right)^2 + \left(los_n \sigma_{v_n}\right)^2 + \left(los_u \sigma_{v_u}\right)^2} \qquad (S6)$$

227
228   where *los* and σ_v are the components of the unit vector and uncertainties for the east, north, and up
229   components. We use the values estimated above of 1.5 and 1.3 mm/yr for σ_{v_e} and σ_{v_u}, respectively,
230   and use a conservative value of 3 mm/yr for σ_{v_n}, as north-south velocities are derived predominately
231   from GNSS. From this information we can then estimate the average uncertainties on the original line-
232   of-sight velocities, which are ~1.4 mm/yr for both the ascending and descending geometry. This
233   compares well to the standard deviation of the residual between the InSAR data and the predicted
234   velocities from the *coarse* velocity model, which has a value of 1.6 mm/yr, and is a more realistic
235   estimate than the formal uncertainties from LiCSBAS, which are typically in the range 0.1 to 0.6
236   mm/yr (95% confidence).
237
238   Finally, we propagate uncertainties in the line-of-sight velocities to uncertainties in east-west and
239   vertical velocities using the standard equations *(67)*, to make maps of the uncertainty in the east and
240   vertical velocities. The final spatial distributions of uncertainties are a function of the number of data
241   sets and the viewing geometries at an individual pixel and range from 1.3 to 2.0 mm/yr and 1.0 to 1.5

242   mm/yr for the eastward and vertical uncertainties, respectively (95% confidence intervals) (Fig. S11).
243   The comparison between InSAR-derived velocities and GNSS/levelling data shows an RMS of 2.2
244   mm/yr for eastward velocity and 1.8 mm/yr for vertical velocity, with 2.2 mm/yr for vertical GNSS and
245   1.7 mm/yr for levelling data, respectively (Fig. S12).
246
247   Our estimates of strain rates for the Sichuan basin (enclosed by the gray dashed line in Fig. S6d), where
248   tectonic deformation is slow, are of 6 nanostrain/yr in shear strain, 1 nanostrain/yr in dilatation, and 9
249   nanostrain/yr in the second invariant of the strain rate – these are likely a combination of a small
250   amount of real strain and noise in the data.
251
252
253   7. Simplified conceptual model analysis
254
255   We obtained numerical solutions (*10*) for deformation of the thin spherical shell using the finite
256   element method with a model geometry that approximates the actual geographical distribution of the
257   India-Asia collision, including variation of rheological properties and disposition of major active faults
258   based on the geodetic strain rate field. The model that best matches the geodetic velocity field obtained
259   by Fang et al. (*10*), and shown in Fig. 3a,b and Fig. S15, generally requires that the major fault systems
260   are weak in terms of the fault resistance coefficient f. To demonstrate more clearly why this is, we
261   consider here a simplified model system which includes only the essential elements of a weak fault
262   bounding a flow driven by an excess of gravitational potential energy.
263
264   We solve the governing equations for the thin viscous sheet in plane Cartesian coordinates, assuming
265   constant viscosity $n = 1$ and $B = 2\eta_0$ in Eq. (1), and no variation of gravitational potential energy Γ
266   within a rectangular region $0 \leq x \leq S, 0 \leq y \leq W$. This domain represents roughly the region
267   bounded in the south by the Himalayas between about 85ºE and the eastern syntaxis, and in the north
268   by the Kunlun Fault system. Similar to the actual displacement field, we represent a velocity field in
269   which the north (y) component of velocity, is approximately zero ($v = 0$ on all 4 boundaries). We set S
270     $= 2W$ as representative of the region and impose $u = v = 0$ on the west ($x=0$) boundary. We also assume
271   that the north ($y=W$) boundary represents a fault on which Eq. (2) applies, with Δu here representing
272   the velocity relative to a rigid external region. We assume in each case that deformation is driven by a
273   constant x-direction "pull" σ_T on the boundary $x = S$, and note also that the external pull can mimic
274   exactly the effect of a step-wise decrease in gravitational potential energy across the east ($x=S$)
275   boundary, $\Delta\Gamma = L\sigma_T$, where L is the lithospheric thickness. For these calculations with constant
276   viscosity, we have used dimensionless variables: for distance $(x', y') = (x, y)/W$, viscosity $\eta' = \eta/\eta_0$,
277   stress $\sigma'_{ij} = \sigma_{ij}/\sigma_T$ and velocity $u' = u\eta/(W \sigma_T)$. The dimensionless fault resistance coefficient is
278   then $f' = (W/\eta)f$.
279
280   Fig. S18 shows the variation of the east (x) component of velocity within the region for various
281   boundary conditions on north and south boundaries. In Case 1 (Fig. S18a) we impose zero shear stress
282     $\tau' = 0$ on both $y' = 0$ and $y' = 1$ boundaries; u' then increases linearly from zero at $x' = 0$ to a
283   maximum velocity $u'_{max} = 1$ on $x' = S/W$. Case 1 serves as a reference value against which the
284   other cases may be compared. For Case 2 ($u' = 0$ on both north and south boundaries; Fig. S18b) the
285   maximum velocity is only about 0.39 and it decays rapidly with distance from the east boundary. For
286   Case 3 (Fig. S18c), with $u' = 0$ on the south boundary and $\tau' = 0$ on the North boundary, the
287   maximum flow velocity reaches about 0.72 on the north-east corner. Relative to Case 2, the stress-free
288   northern boundary mobilises a much more extensive part of the region to participate in the flow, mainly
289   in the region adjacent to that boundary. Cases 1 to 3 are consistent with the fault condition on the

7

290   northern boundary if $f' = 0$ (Case 3) or $f' \rightarrow \infty$ (Case 2), and we show three more cases (Fig. S18d,e,f)
291   with $f' = 0.2$, 1 and 5 respectively which, as expected, show solutions that are gradational between
292   Cases 2 and 3. The fault-like boundary condition clearly enables a much greater part of the region
293   away from the $x = S$ boundary to be activated for eastward flow as f' is decreased. The approximate
294   analytic solutions described in the next section explain the change in effective length scale of the
295   solution, from S in Case 1 to W in Case 2, to $2W$ in Case 3.
296
297   Fig. S19a shows the systematic variation of $u'(y')$ at $x' = 1.75$, for f' between 0.05 and 10, together
298   with the limiting cases of $f' = 0$ and $f' \rightarrow \infty$. We see that in Fig. S19a, $f' \approx 2$ results in the slip
299   velocity on the $y' = 1$ boundary reaching about half of the amplitude obtained for the zero shear-stress
300   case. When scaled to dimensional values, the magnitude of the velocity depends on viscosity and
301   boundary traction also, but the shape of the y (north-south) profile of the x (east) component of velocity
302   is simply diagnostic of the magnitude of f' on the northern boundary. We repeated the calculations
303   using a non-linear rheological law representative of depth-averaged lithospheric deformation with $n =$
304   3, and constant coefficient B. Comparison of Fig. S19a ($n = 1$, constant viscosity) and Fig. S19b ($n =$
305   3, power-law viscosity) shows that in both cases the fault-like boundary condition has a similar impact
306   as f is varied between 0 and ∞. For both $n = 1$ and $n = 3$, the maximum velocity for Case 2 is about
307   half that for Case 3, but it is clear for Case 2 that the velocity decays more quickly with distance from
308   the $x = S$ boundary for $n = 3$, as found by (68).
309
310
311
312
313   <u>8. Related analytical solutions for thin viscous sheet model</u>
314
315   In what follows we provide approximate analytical solutions for the constant viscosity case that shed
316   light on the results of the preceding section. The x-component of the thin viscous sheet formulation for
317   the simplified problem may be expressed:
318
319    $$2\frac{\partial \tau_{xx}}{\partial x} + \frac{\partial \tau_{yy}}{\partial x} + \frac{\partial \tau_{xy}}{\partial y} = \frac{1}{L}\frac{\partial \Gamma}{\partial x} \tag{S7}$$
320
321   where Γ is the gravitational potential energy, L is the thickness of the sheet, and $\tau_{\alpha\beta}$ are the
322   components of the depth-averaged horizontal stress tensor in the (x,y) plane. If we assume a
323   Newtonian viscous constitutive law with viscosity η, and negligible motion in the y-direction we obtain
324   the following differential equation for the eastward component of velocity:
325
326    $$4\frac{\partial^2 u}{\partial x^2} + \frac{\partial^2 u}{\partial y^2} = \left(\frac{1}{\eta L}\right)\frac{\partial \Gamma}{\partial x} \tag{S8}$$
327
328   If we ignore gradients of gravitational potential energy within the plateau, the equation is reduced to a
329   simple homogeneous partial differential equation, and separation of variables gives the following
330   general solution:
331
332    $$u(x,y) = \left[A\cosh\left(\frac{Cx}{2}\right) + B\sinh\left(\frac{Cx}{2}\right)\right]\left[E\cos(Cy) + F\sin(Cy)\right] + Dx + Gy + Hxy \tag{S9}$$
333
334   and the shear stress τ_{xy} is:
335

$$\tau_{xy} = \eta C[\sinh(\tfrac{Cx}{2})][-E\sin(Cy) + F\cos(Cy)] + \eta Hx \qquad \text{(S10)}$$

where C^2 is a separation constant that is constrained by boundary conditions, along with the other integration constants A, B, D, E, F, G and H that are determined when the boundary conditions are specified. We obtain approximate solutions for the domain $0 \le x < S$ and $0 \le y \le W$, and assume that deformation is driven by an x-direction "pull" σ_T on the boundary $x = S$, noting that the external pull can represent the effect of a step-wise decrease in gravitational potential energy across this boundary.

For Case 1 in which zero shear stress is applied to the boundaries $y = 0$ and $y = W$, and $C = 0$

$$u(x) = \frac{\sigma_T S x}{4\eta} \qquad \text{(S11)}$$

as illustrated in Fig. S18a.

For Case 2 in which the velocity on both horizontal boundaries is zero: (Fig. S18b) and $C = \pi/W$, so

$$u = \frac{W\sigma_T}{2\pi\eta}\left[\frac{\sinh(\pi x/(2W))}{\cosh(\pi S/(2W))}\right][\sin(\tfrac{\pi y}{W})] \qquad \text{(S12)}$$

if the outward pull on $x = S$ is:

$$\sigma_{xx} = \sigma_T \sin(\tfrac{\pi y}{W}) \qquad \text{(S13)}$$

As in the preceding case, the peak amplitude is proportional to the magnitude of the boundary force and inversely proportional to viscosity. However, contrary to Case 1, $u_{\max}$ is approximately proportional to W (rather than S). The effect of neglecting the y-component of velocity in deriving Eq. (S12) means that (S12) underestimates the maximum u in the 2D solution by about 7%. For Fig. S18 we used the same constant traction boundary condition on $x = S$ in each Case, in order that our comparison of rate and distribution of the outward flow is due only to changes of the y boundary conditions. Higher harmonics ($C = 3\pi/W$, $5\pi/W$, etc.) are then present in the solution because of the constant boundary traction we use, but they have only a minor effect on the velocity near the boundary and decay rapidly with distance into the solution domain. Relative to the case where the forcing traction is constant in y, (S13) underestimates the maximum displacement rate by about 18%.

In Case 3 the mix of boundary types with zero velocity on $y = 0$ and zero shear stress on $y = W$ (Fig. S18c) requires that $C = \pi/(2W)$, so both the y-direction wavelength and the decay of velocity in the x-direction are doubled relative to Case 2, and the solution has the form:

$$u = \frac{W\sigma_T}{\pi\eta}\left[\frac{\sinh(\pi x/(4W))}{\cosh(\pi S/(4W))}\right][\sin(\tfrac{\pi y}{2W})] \qquad \text{(S14)}$$

for the boundary traction

$$\sigma_{xx} = \sigma_T \sin(\tfrac{\pi y}{2W}) \qquad \text{(S15)}$$

For those cases in which we assume that shear stress is proportional to u on the north boundary, with fault resistance coefficient f, we take the ratio of shear stress and velocity on $y = W$ to obtain:

9

381

$$\frac{\tan(CW)}{C} = \frac{\eta}{f} \tag{S16}$$

383
384   and the smallest value of C for which that equation holds $(\pi/(2W) \le C \le \pi/W)$ provides the
385   fundamental harmonic for arbitrary f.   Allowing for the different wave-number C, the solution for
386   arbitrary f appears similar to the solution for Case 3 (Eq. S14) but, as Fig. S19 and Fig. 3d indicate, the
387   maximum eastward velocity on $x = S$ decreases smoothly and the location of that maximum moves
388   from $(x, y) = (S, W)$ to $(x, y) = (S, W/2)$, as f varies from 0 to ∞.
389
390

391

392
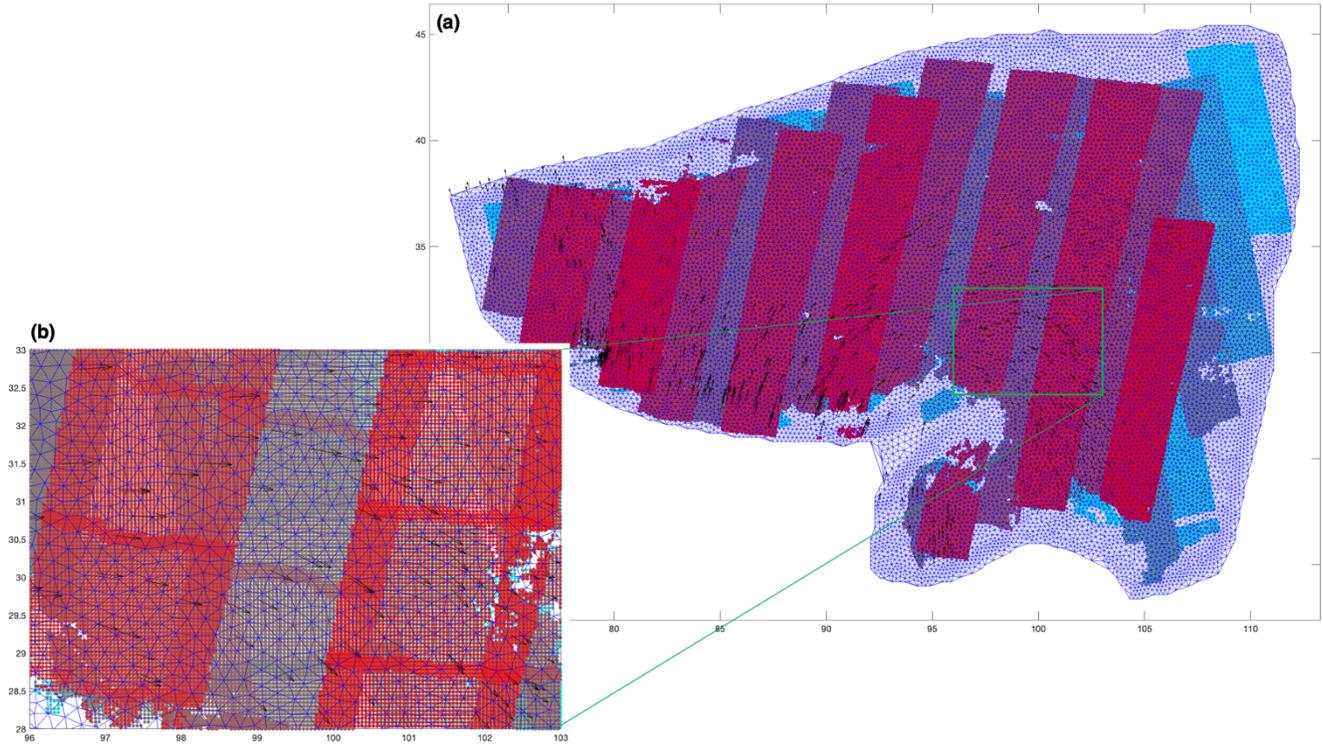
Fig. S1

(a) Mesh and data used for the *coarse* velocity model inversion. The blue lines show the element of the triangular mesh, with black arrows showing the GNSS data used (see Fig. S2). Colored dots show the location of coherent InSAR data used in the inversion. Different tracks are shown in different colors; colors have no other meaning. (b) Close-up of the mesh corresponding to the green rectangle shown in (a).

400

401

402

403
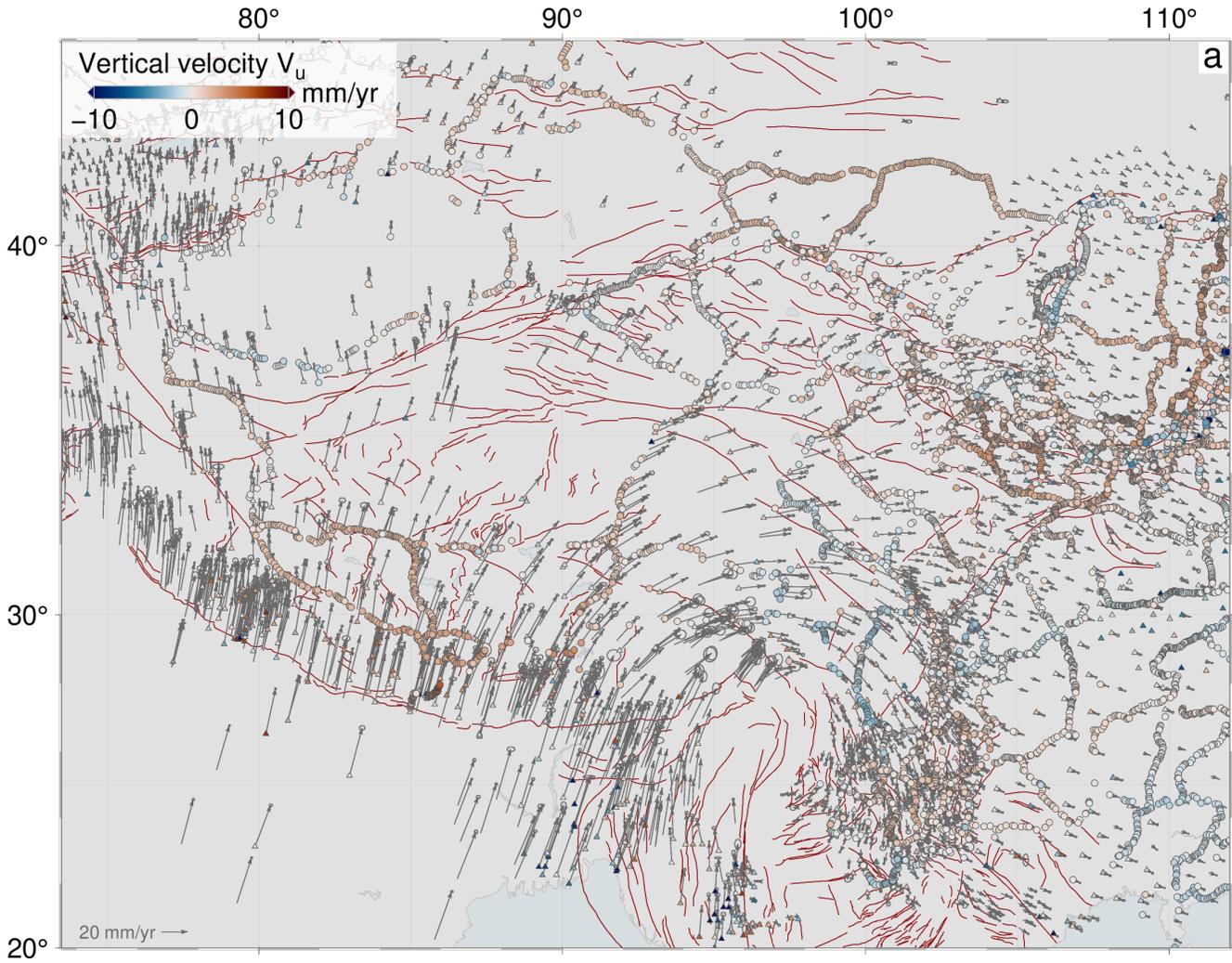
Fig. S2

Compilation of GNSS and levelling velocities in the study region (available at *66*), rotated into the
Eurasia reference frame defined by *(76)*. Vectors show horizontal motion. Colors show vertical
velocities, with constraints from GNSS shown as triangles and levelling measurements as circles (red is
uplift).
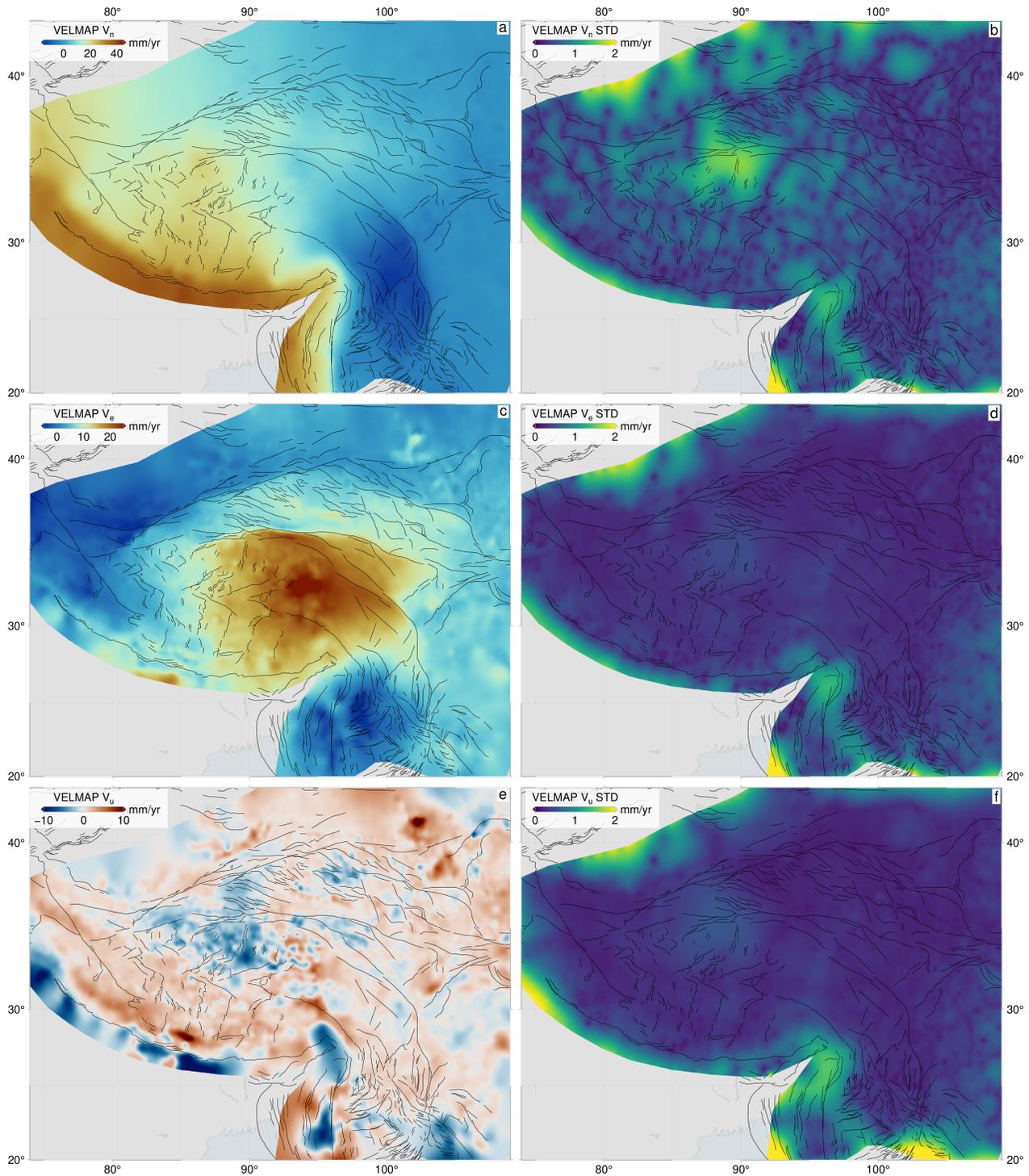
Fig. S3

The 3D *coarse* velocity model, obtained by joint inversion of InSAR and GNSS data to give velocities on the nodes of the triangular mesh (Fig. S1). (a) Northward velocity (positive values are towards north), (c) Eastward velocity (positive values are towards east), (e) Vertical velocity (positive values are uplift). Black lines show active faults from the Global Earthquake Model (*65*). The right column shows the spatial distribution of uncertainties (1 standard deviation) of the (b) northward, (d) eastward, and (f) vertical velocity components of the velocity field.

13

418

419
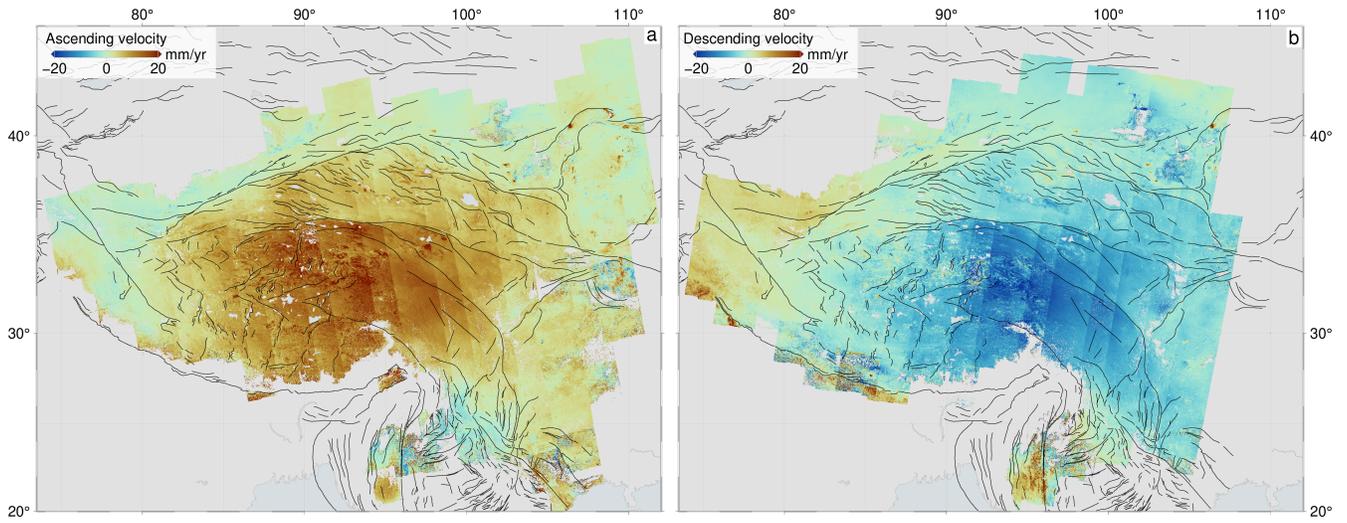
Fig. S4

Line-of-Sight (LOS) velocity mosaics in (a) ascending and (b) descending geometries for study area in a Eurasian Reference frame defined by GNSS. Positive indicates motion away from the satellite.
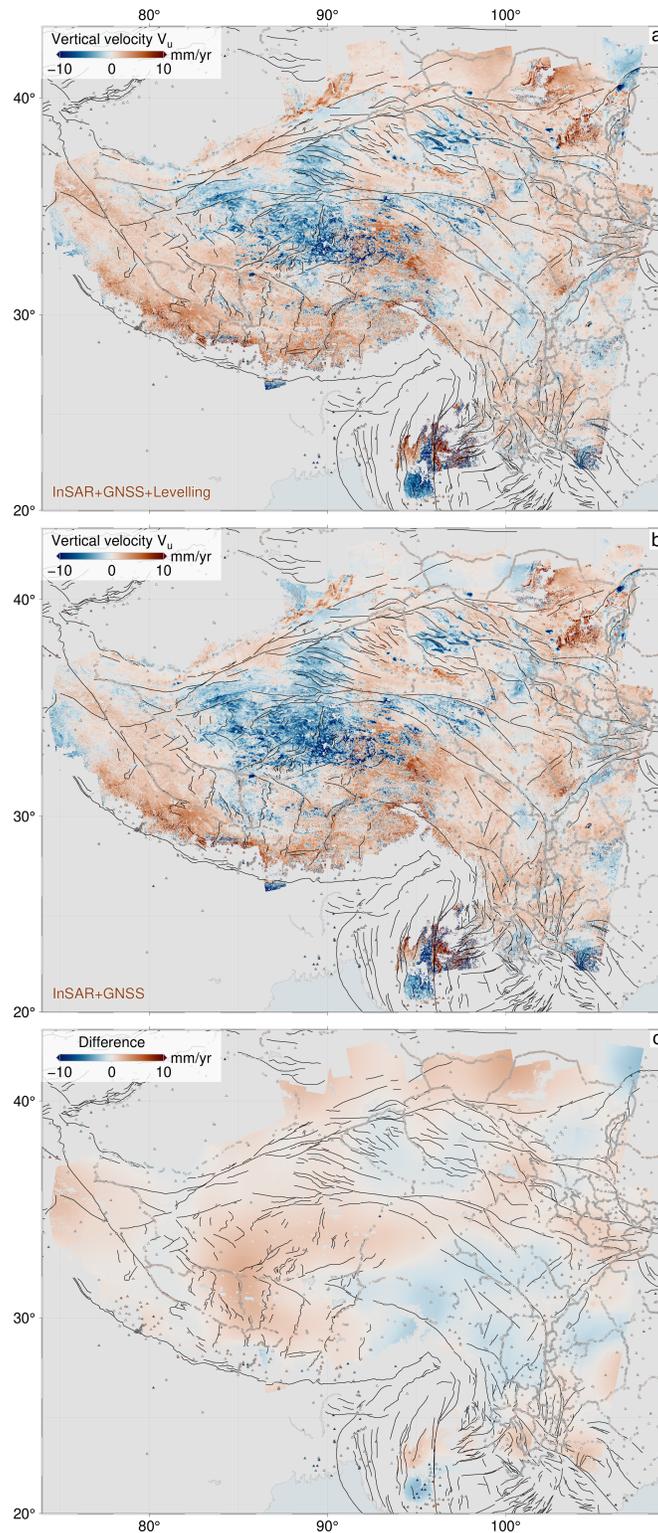
Fig. S5

Vertical velocity field for the Tibetan plateau at 1 km resolution, derived from combination of ascending and descending InSAR data shown in Fig. S4. (a) Vertical velocity field derived from inversion using vertical GNSS (colored triangles) and levelling (circles) data as constraints. (b) Vertical velocity field derived from inversion without using levelling data. (c) Difference between (a) and (b).
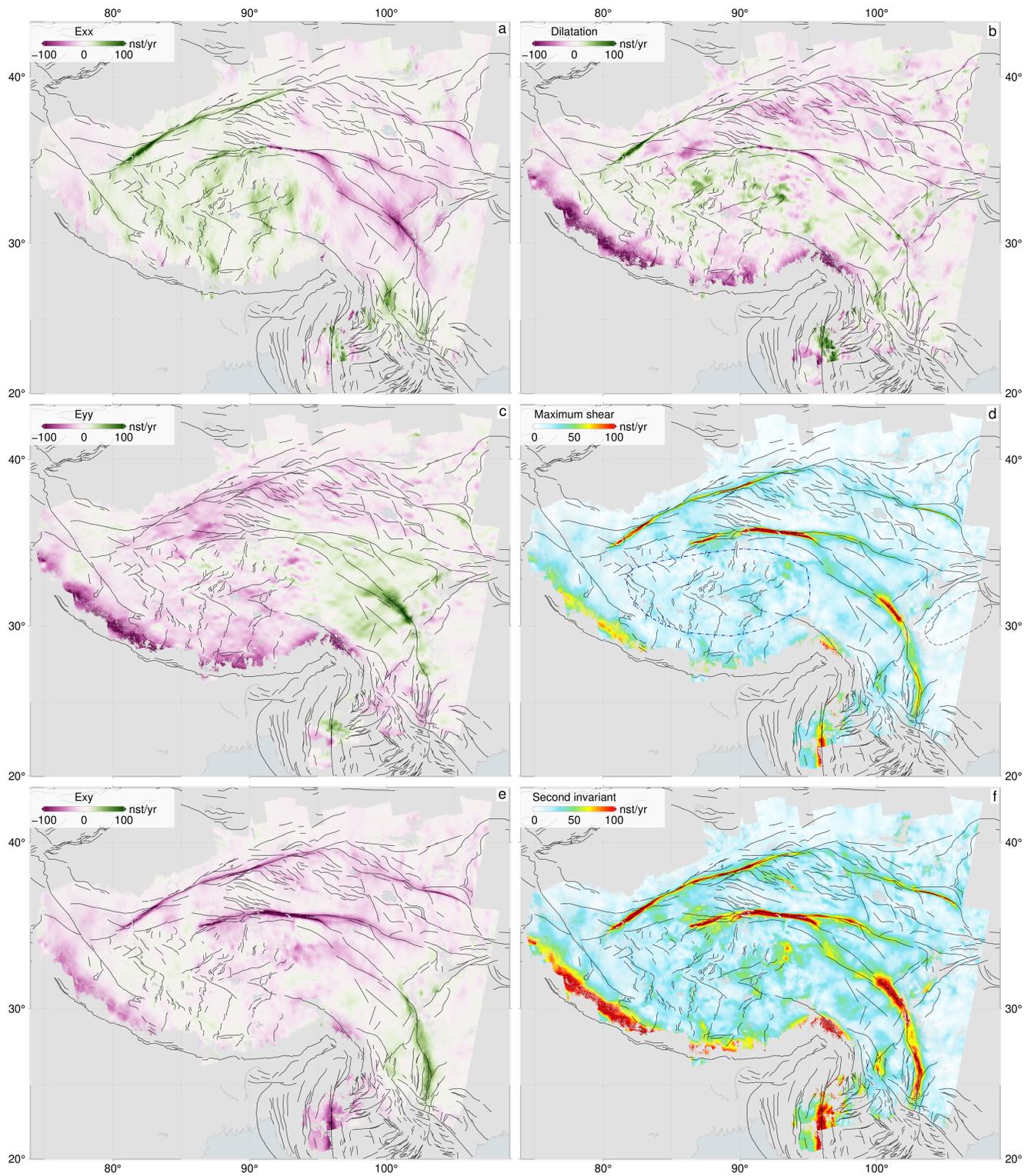
15

Fig. S6

Components of the horizontal strain rate tensor derived from the gradients of InSAR eastward and interpolated GNSS northward (Fig. S3a) velocities. Inset on each panel gives the component and color scale.

16

436

437
438
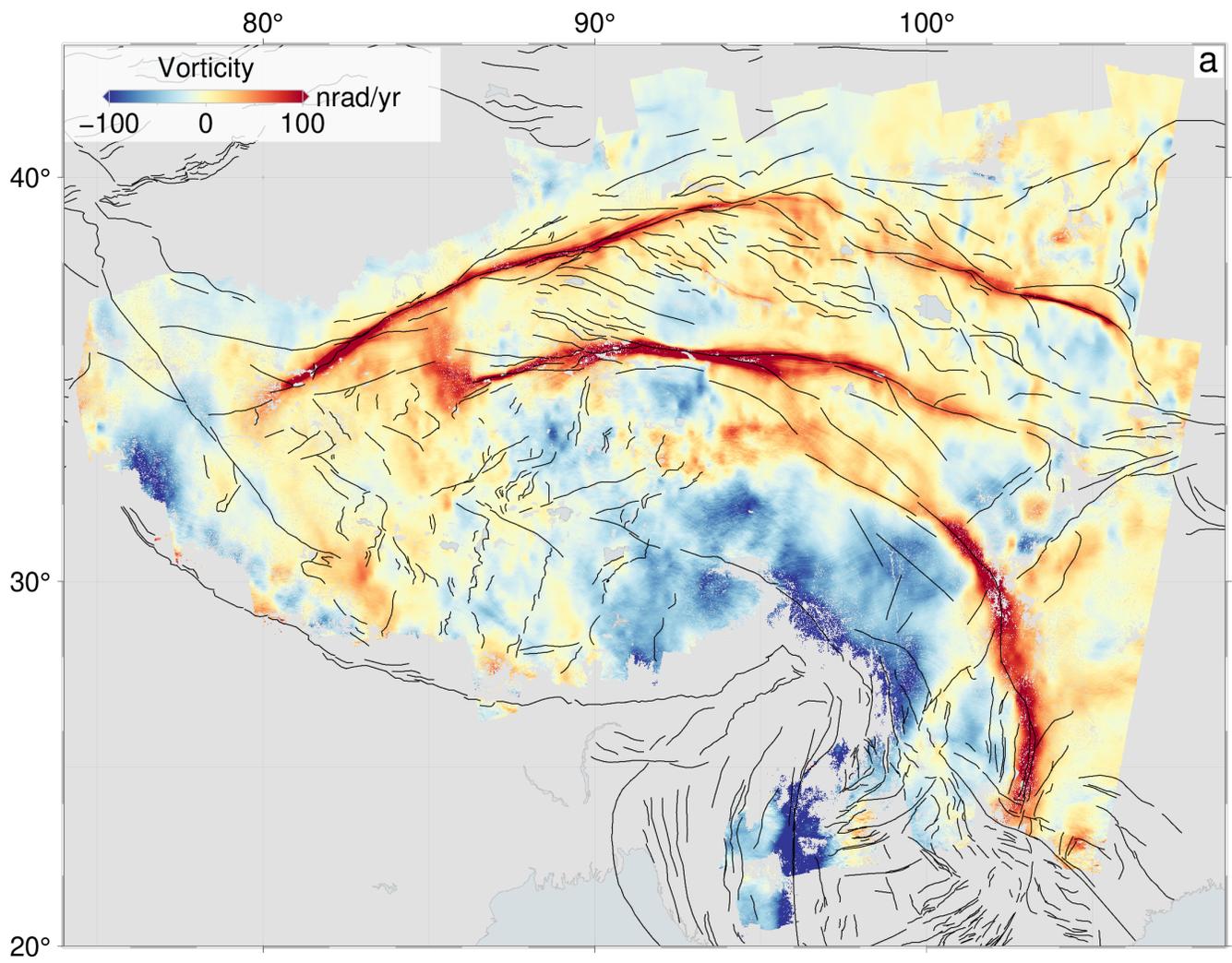
Fig. S7

Vorticity, with positive values indicating anti-clockwise rotation.

441
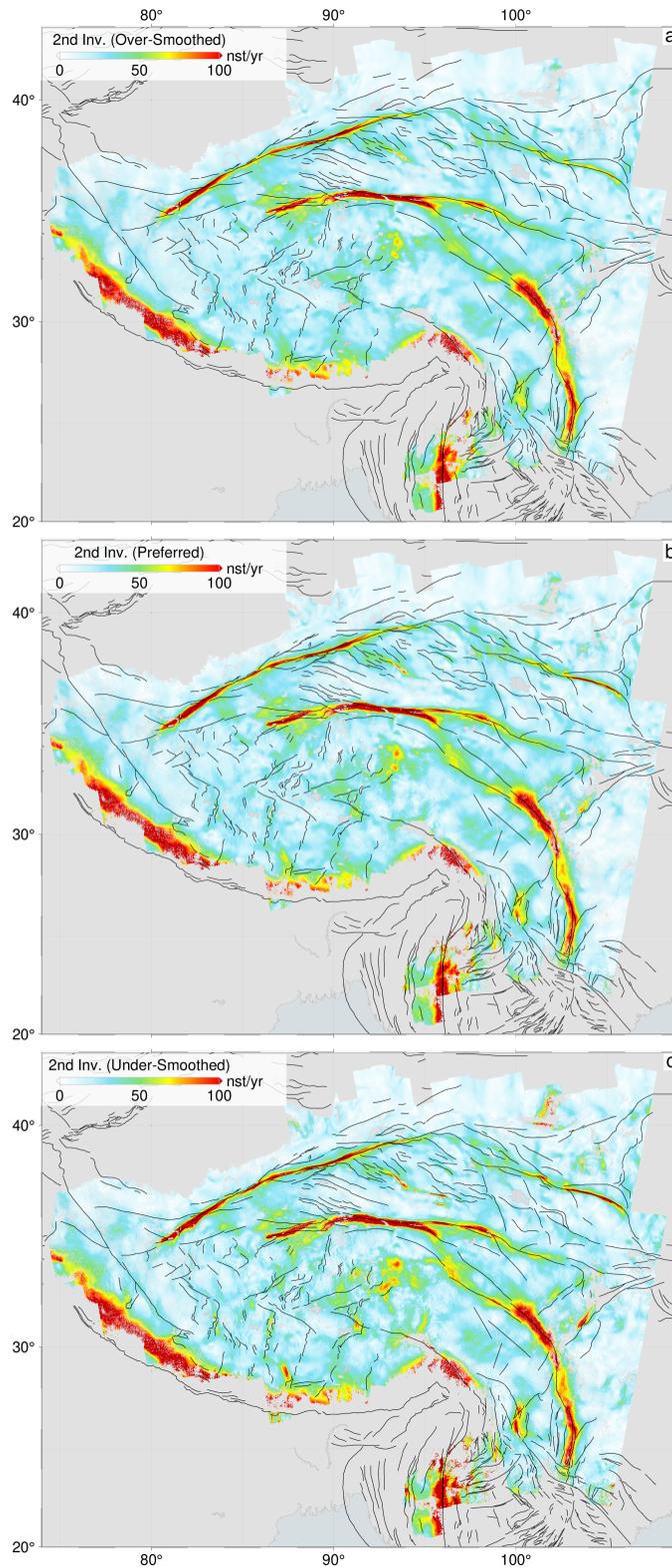
Fig. S8

Second invariant strain rate fields using different smoothing parameters for the east-west velocities. (a) uses a median filtering window size of 200 km and is over-smoothed. (b) uses a window size of 150 km and is our preferred solution. (c) uses a window size of 100 km and is under-smoothed.

446
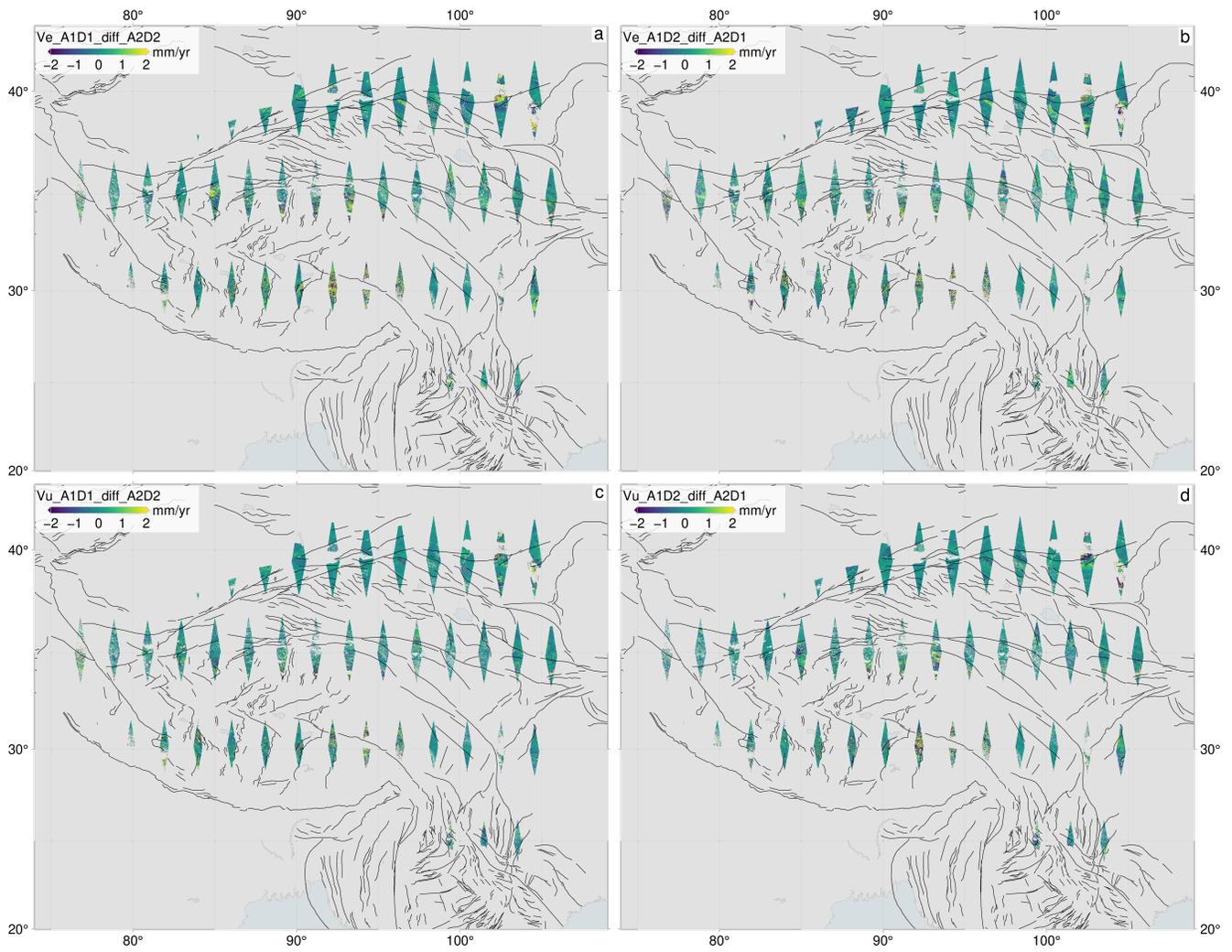
Fig. S9

Difference maps between independent estimates of east-west and vertical velocities, for pixels where 4
independent observations (2 ascending and 2 descending) exist.

19

452

453
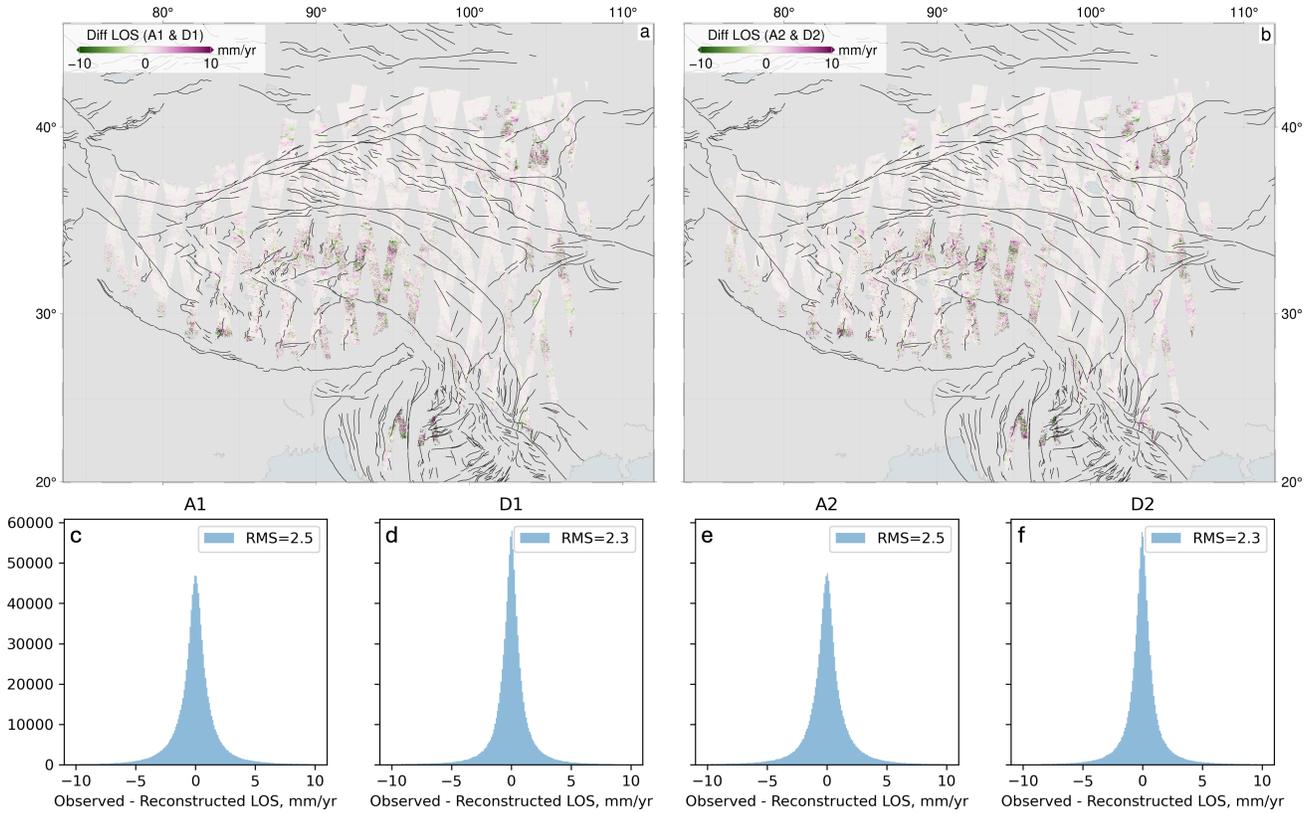
Fig. S10

LOS uncertainty analysis assessed by comparing observed and reconstructed LOS velocities at track overlaps. The observed LOS velocity field shown in Fig. S4 is divided into four non-overlapping groups of ascending and descending tracks: A1, A2, D1, and D2. (a–b) A1 represents the differences between the observed LOS velocities in A1 and the reconstructed LOS velocities at A1's pixel locations, derived using the LOS velocities from A2, D1, and D2. The same reconstruction approach is applied for D1, A2, and D2, respectively. (c–f) Residuals and root-mean-square (RMS) differences between the observed and reconstructed LOS velocities for each corresponding track group.

454
455
456
457
458
459
460
461
462
463
464

465

466
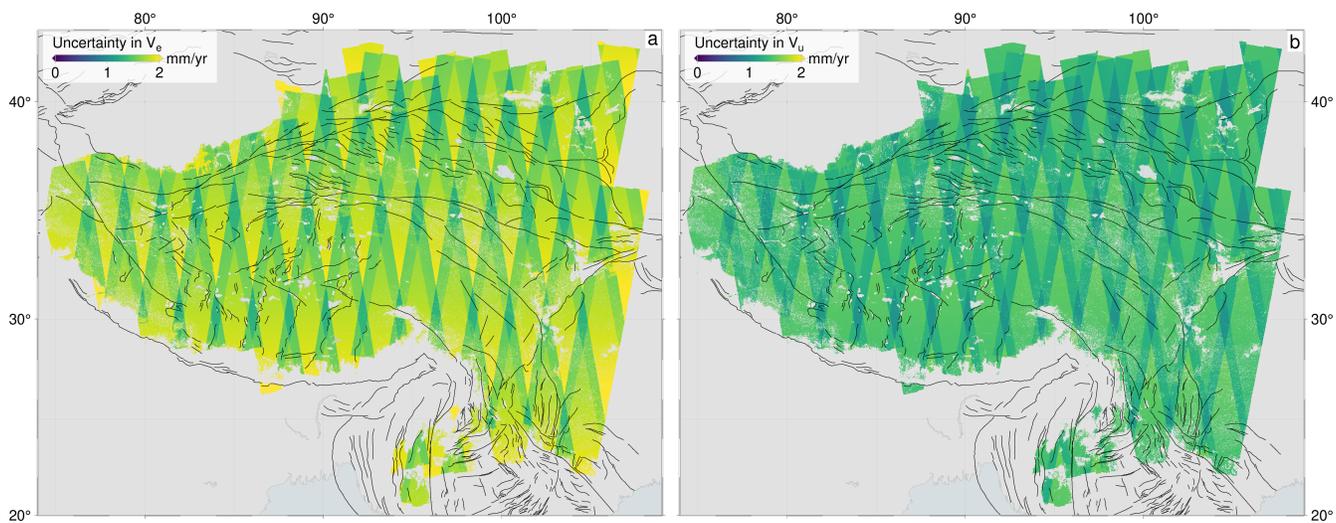
Fig. S11

Estimates of uncertainty (1σ) for 1 km grids of (a) east (V_e) and (b) vertical (V_u) velocities.

470

471
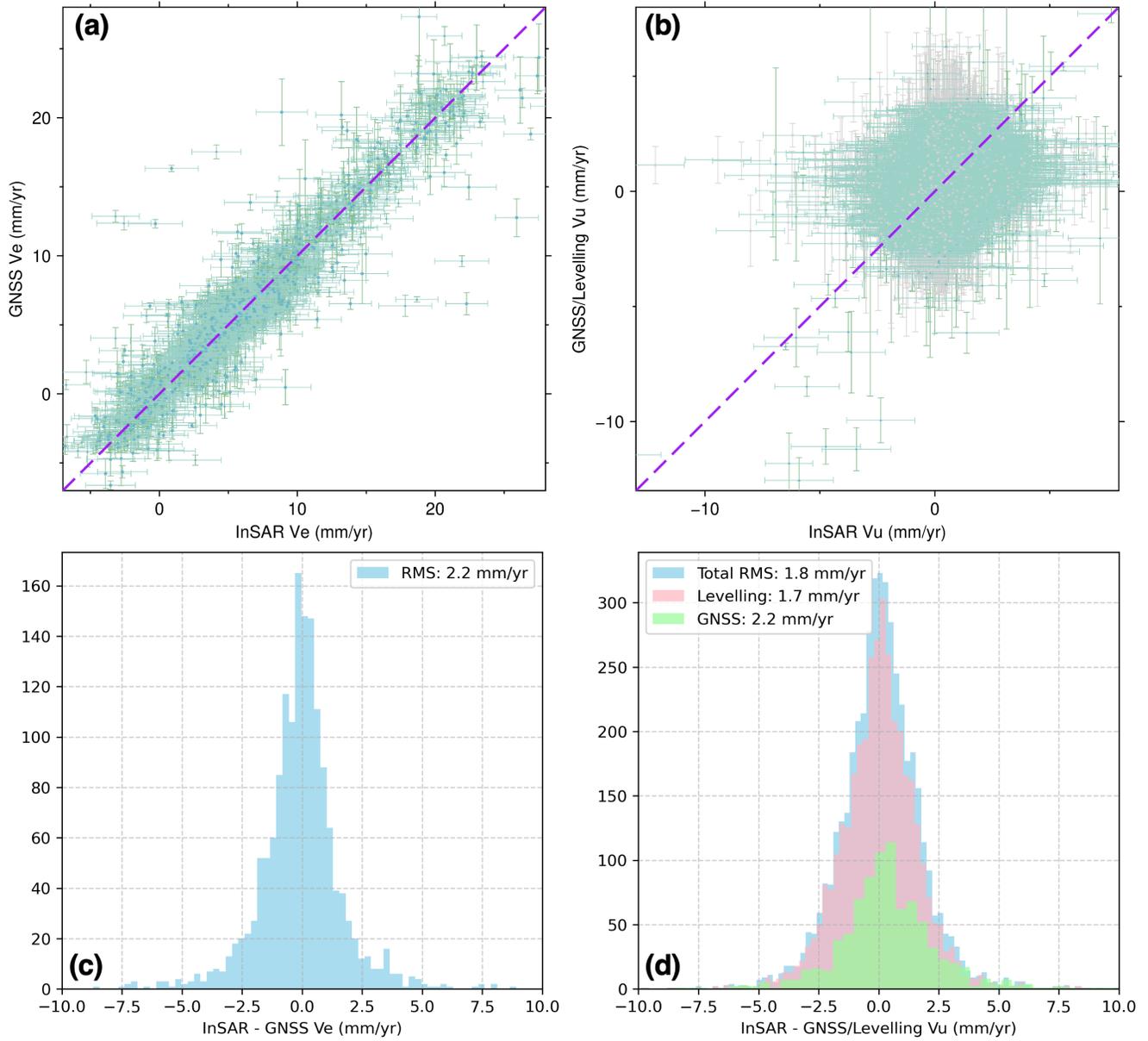
Fig. S12

Correlation plot of InSAR-derived (a) V_e and (b) V_u against (a) GNSS V_e and (b) GNSS/levelling V_u. Levelling data are denoted by gray bars. Purple dashed lines are one-to-one line for reference. The corresponding histograms of mismatch are shown in panels (c)-(d).

476

477
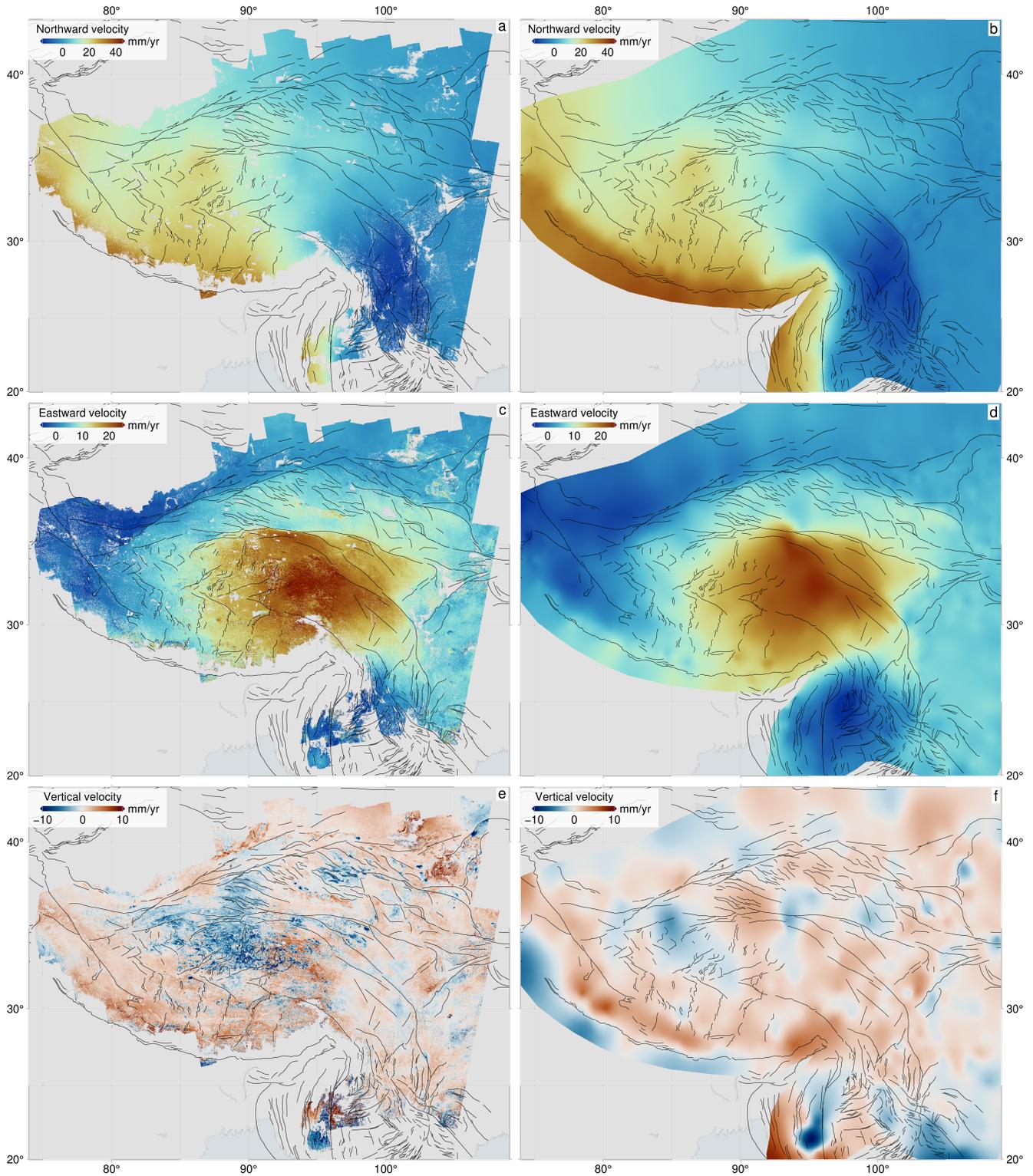
Fig. S13

(a, c, e) 3D velocities derived through the inclusion of InSAR data, and (b, d, f) velocities constrained by GNSS and levelling observations only. Inset in each panel indicates the component and color scale.

23

481
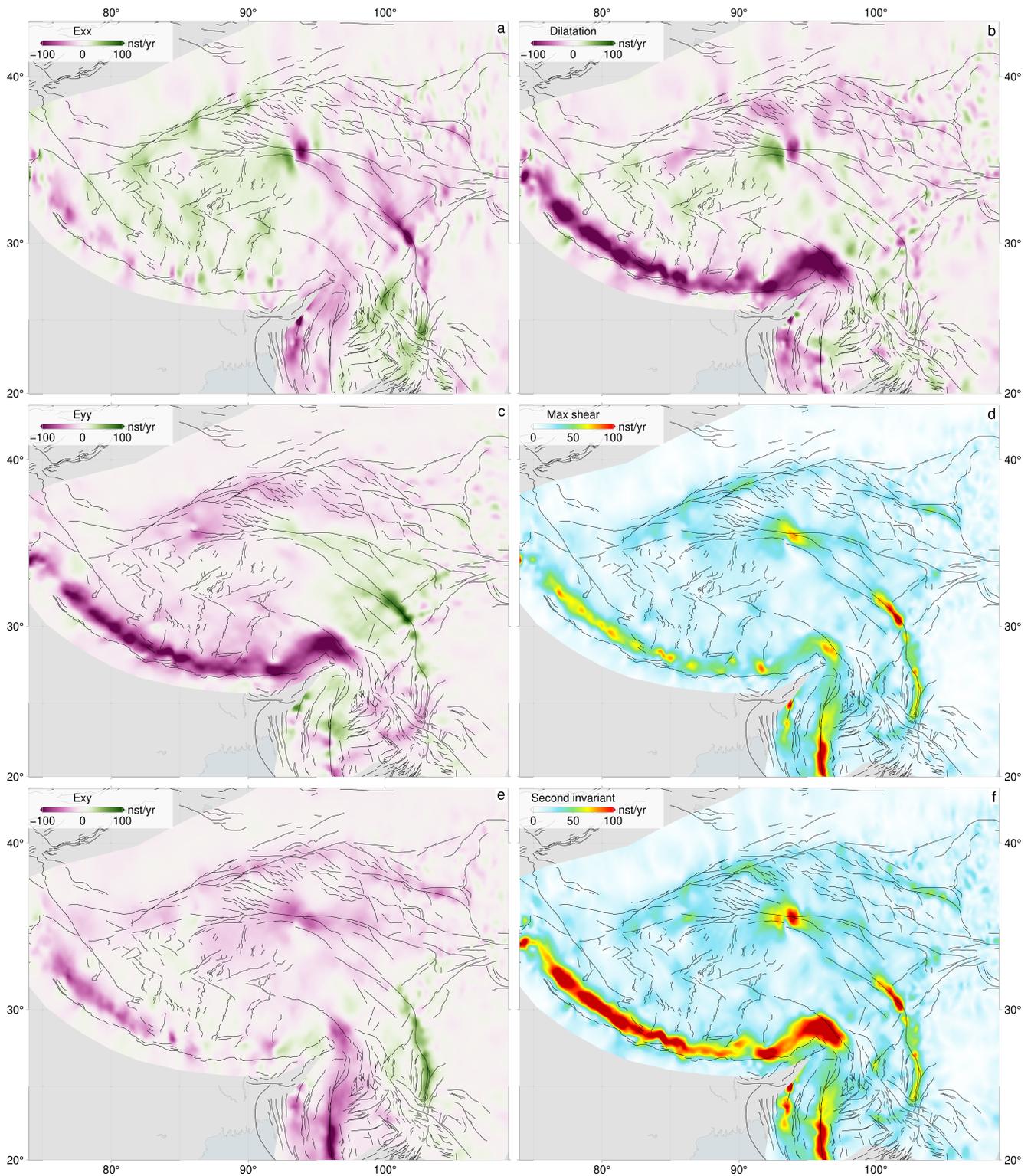
482
483 **Fig. S14**

484 Components of the horizontal strain rate tensor derived from the gradients of interpolated GNSS
485 horizontal velocities (Fig. S13b,d). See Fig. S6 for comparison with results obtained through the
486 inclusion of InSAR data.

24

487
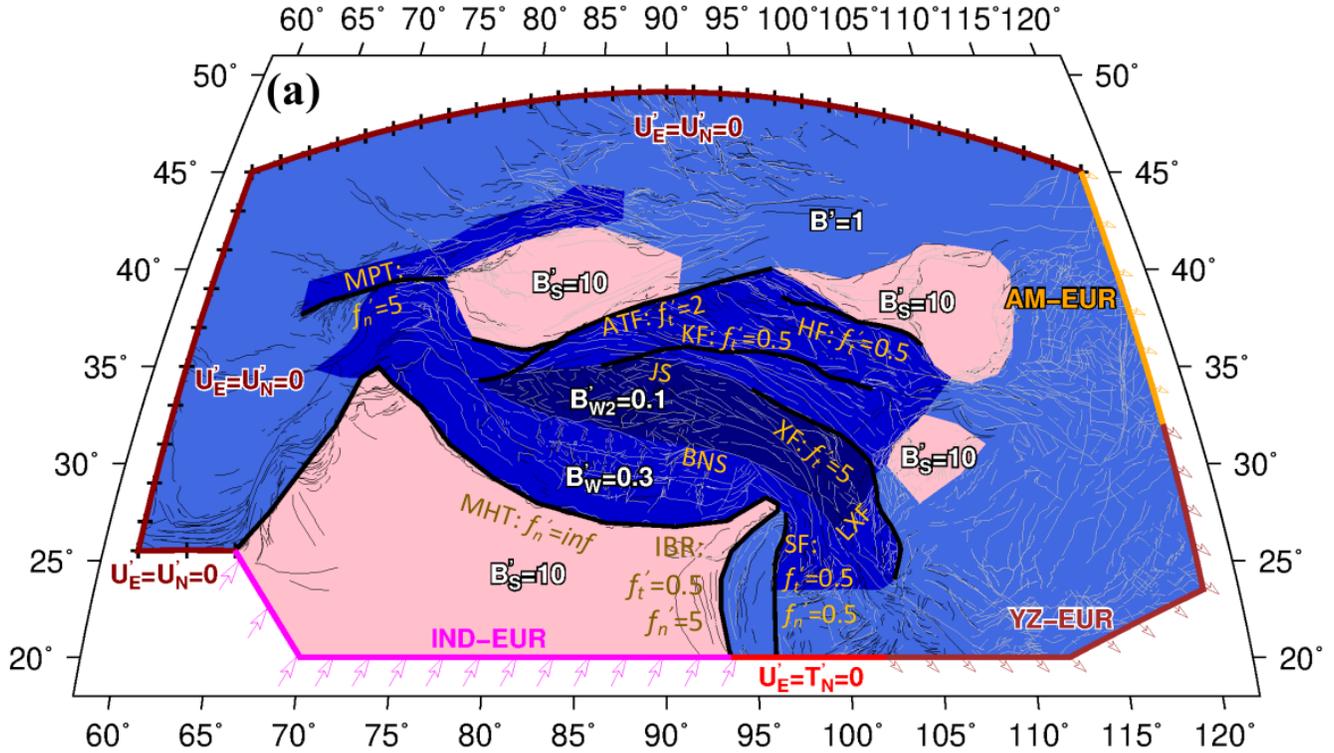
Fig. S15

Boundary and internal conditions for the dynamic faulted thin viscous shell model after (*10*). The maroon outer boundary with black tick marks is held fixed with zero velocity, where the other boundaries are given velocities imposed by far-field plate motion poles of rotation for the Indian (IND), Yangtze (YZ), and Amur (AM) plates relative to Eurasia (EUR), except for the small region east of India marked in red, where the eastward velocities and northward tractions are set to zero. Colors mark regions with different dimensionless viscosity coefficient, labeled as *B'*, relative to background far-field values *B'* = 1; pink areas are strong, and dark blue areas are weaker than average. Thick black lines are the faults that are allowed to slip in this model with values of the dimensionless fault-resistance coefficient *f'* on each fault determined by systematic comparison of model velocity field with observed geodetic velocity sampled from Fig. S3. Viscous flow equations were solved using the 2D finite-element code, *basil* (*10,43*). Details of how parameters are made dimensionless are given in *(10)*. Model faults: ATF, Altyn Tagh Fault; HF, Haiyuan Fault; IBR, Indo-Burma Ranges; KF, Kunlun Fault; MHT, Main Himalayan Thrust; MPT, Main Pamir Thrust; SF, Sagaing Fault; XF, Xianshuihe Fault.

25

505
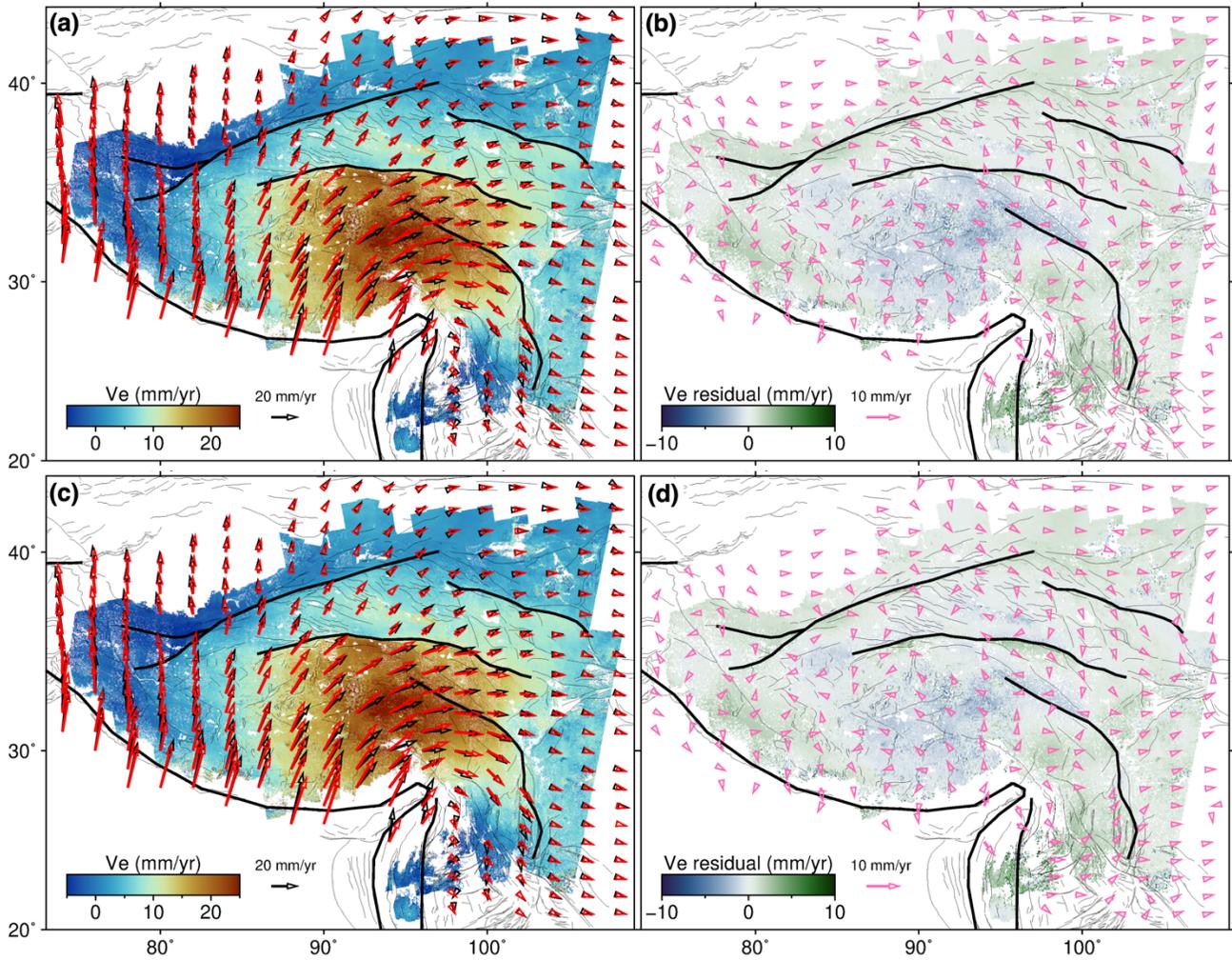
Fig. S16

Observations, dynamic model predictions, and residuals for horizontal velocities. (a, c) Eastward velocities (Ve), overlaid with observed (black, sampled from Fig. S3a,b) and modelled (red) velocity vectors. (b, d) Residual Ve field, with residual velocity vectors shown as pink arrows. (a, b) show results for our preferred model with f'=0.5 applied to the Kunlun Fault, while (c, d) show results for a test model with f=0 on the Kunlun Fault.
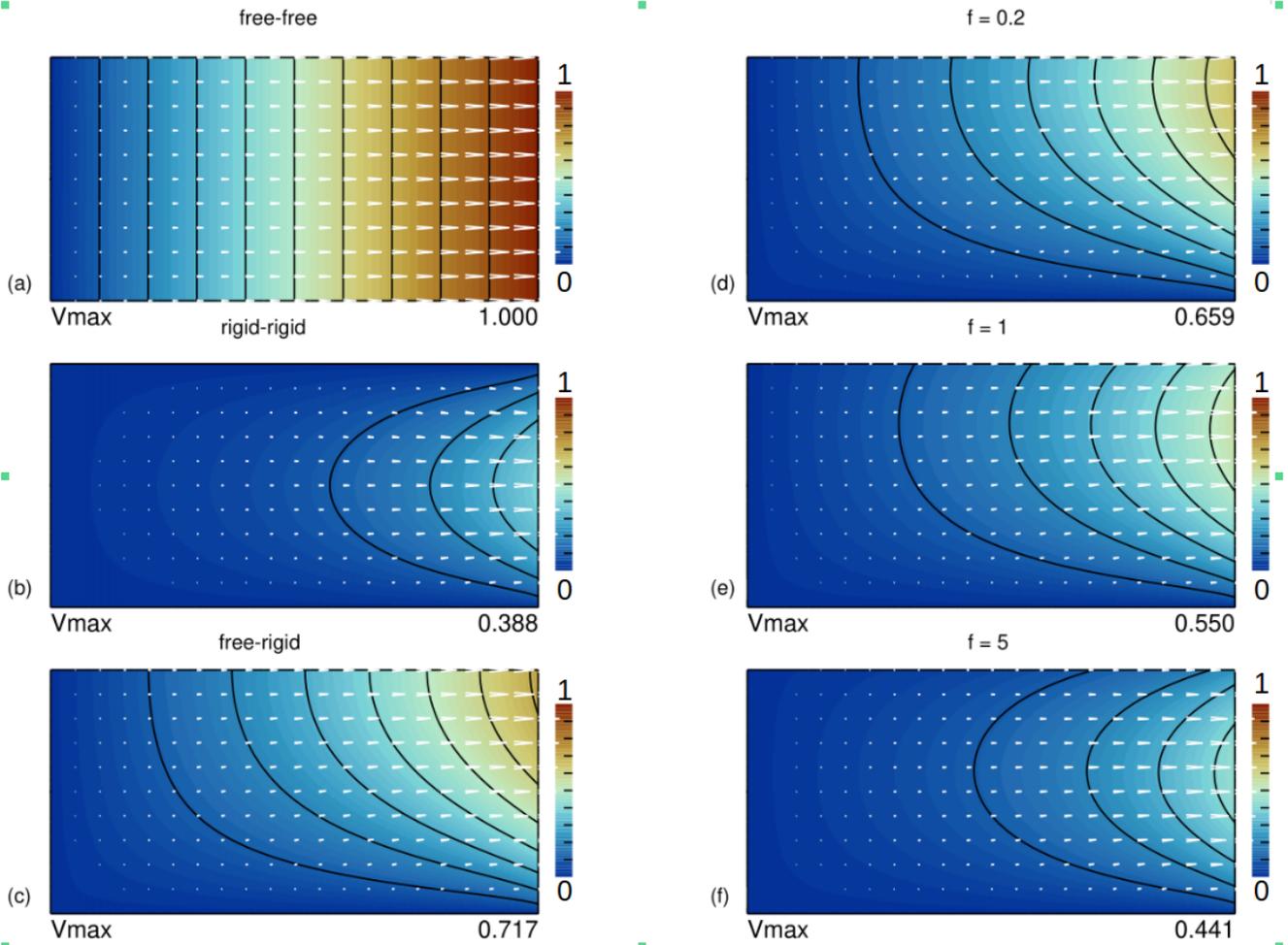
513
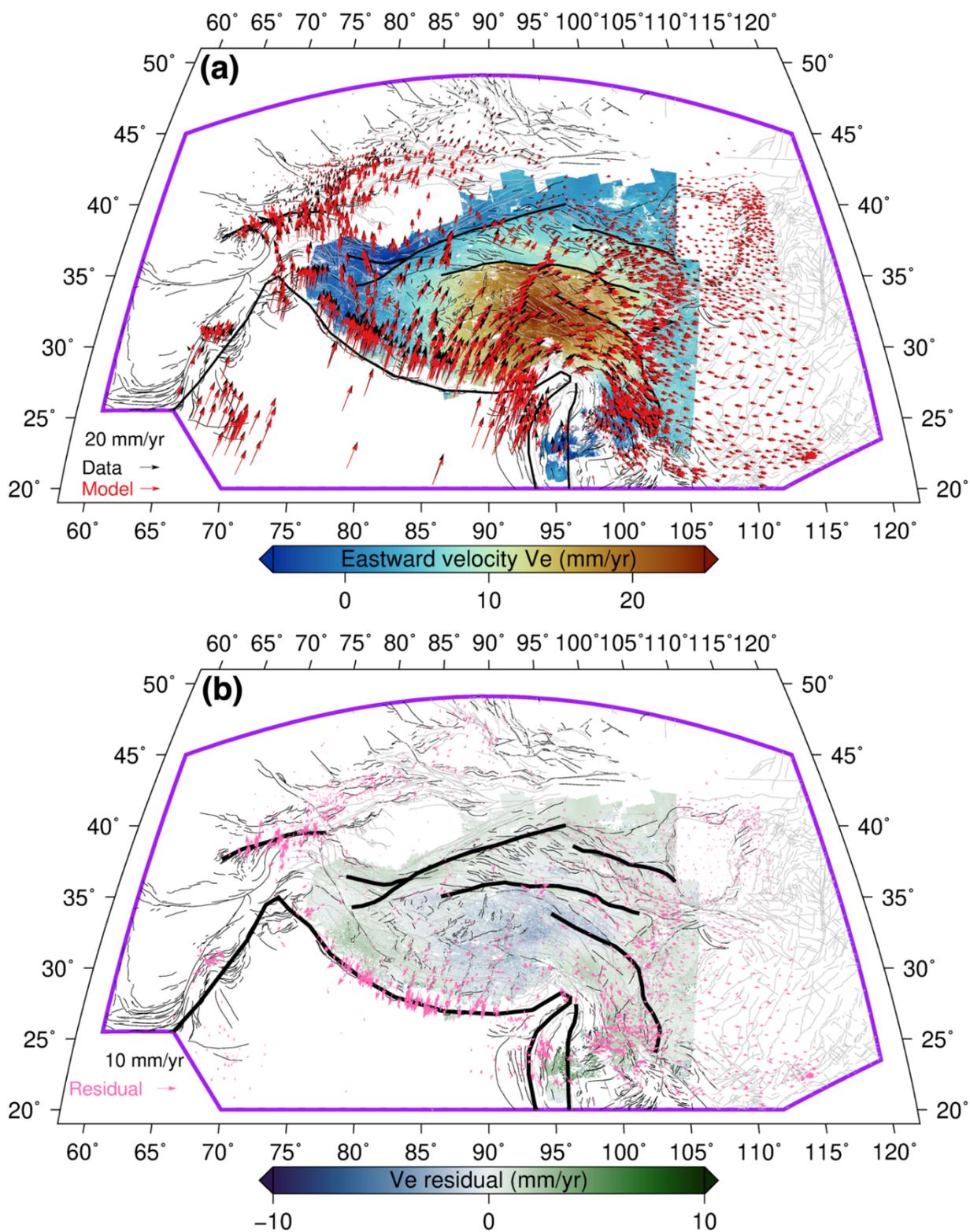
Fig. S17

Same as Fig. S16a,b, but overlaid with observed and modelled GNSS horizontal velocities (a) and residuals (b).

517
518

520 **Fig. S18**

521 Maps of the x-component of velocity in the domain $0 \leq x \leq S = 2$ and $0 \leq y \leq W = 1$ for different
522 boundary conditions in the case of $n = 1$ and uniform viscosity. In all cases the y-component of
523 velocity is zero on all 4 boundaries, the x=0 boundary is rigid, and the x=S boundary has an applied
524 outward normal traction $\sigma_T = 1$ that is constant in y. For all except (a) the boundary y=0 is free. The
525 two horizontal boundaries are zero shear-stress for (a) and zero velocity for (b). The boundary y=W is
526 zero stress for (c), and (d-f) use fault resistance coefficient $f' = 0.2$ (d), 1 (e) and 5 (f). The maximum
527 velocity in each panel (Vmax) is indicated by the number in the bottom right.

528
529

28

530
531

532
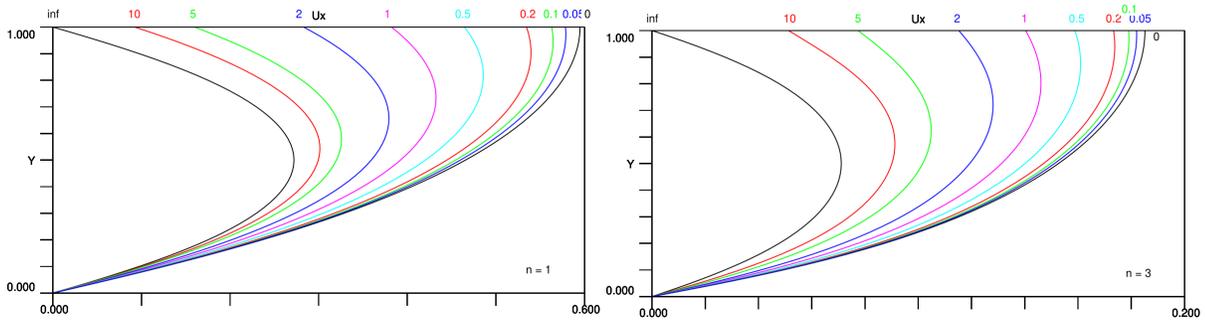
Fig. S19

Profiles of the *x*-component of velocity along the line *x* = 1.75 for (left) constant viscosity (as Fig. S18*b-f*) and (right) for similar calculations using power-law flow with *n* = 3. The value of *f'* applied to the north boundary is indicated for each profile.

537

29

References:

(The following references only appear in the supplement. References 1-66 are listed in the main manuscript)

67.   T. Wright, B. Parsons, Z. Lu, Toward mapping surface deformation in three dimensions using InSAR. *Geophys. Res. Lett.* **31** (2004)

68.   P. England, G.A. Houseman, L.Sonder, Length scales for continental deformation in convergent, divergent, and strike-slip environments: Analytic and approximate solutions for a thin viscous sheet model, *J. Geophys. Res. Solid Earth* **90**, 3551-3557 (1985).

69.   Yu, C., Li, Z., Penna, N. T., Crippa, P., Generic atmospheric correction model for interferometric synthetic aperture radar observations, *J. Geophys. Res. Solid Earth* **123**(10), 9202-9222 (2018).

70.   Z. Yunjun, Fattahi, H., Pi, X., Rosen, P., Simons, M., Agram, P., Aoki, Y., Range geolocation accuracy of C-/L-band SAR and its implications for operational stack coregistration. *IEEE Trans. Geosci. Remote Sens.* **60**, 1-19 (2022).

71.   X. Xu, Sandwell, D. T., Toward absolute phase change recovery with InSAR: Correcting for earth tides and phase unwrapping ambiguities. *IEEE Trans. Geosci. Remote Sens.* **58**(1), 726-733 (2019).

72.   P. Wessel, Luis, J. F., Uieda, L. A., Scharroo, R., Wobbe, F., Smith, W. H., Tian, D., The generic mapping tools version 6. *Geochem. Geophys. Geosyst.* **20**(11), 5556-5564 (2019).

73.   M. Lazecky, Fang, J., Hooper, A., Wright, T., Improved phase unwrapping algorithm based on standard methods. In *IGARSS 2022-2022 IEEE International Geoscience and Remote Sensing Symposium* (pp. 743-746). IEEE (2022).

74.   O. L. Stephenson, *et al.*, The impact of plate motions on long-wavelength InSAR-derived velocity fields. *Geophys. Res. Lett.* **49**(21), e2022GL099835 (2022).

75.   J. Elliott *et al*., Deformation, Strains and Velocities for the Alpine Himalayan Belt from transcontinental Sentinel-1 InSAR & GNSS. EarthArXiv eprints (2025): https://doi.org/10.31223/X5GX6B.

76.   Z. Altamimi, *et al.*, ITRF2014 plate motion model. *Geophys. J. Int.* **209**, 1906–1912 (2017).

77.   A. Love, A treatise on the mathematical theory of elasticity. Courier Corporation, (1944).

78.   J. Fang *et al*., Strain partitioning in the Southeastern Tibetan Plateau from kinematic modeling of high-resolution Sentinel-1 InSAR and GNSS. Geophysical Research Letters, **51**(19), 2024GL111199 (2024).